



Review

Smart Polymers for Soft Materials: From Solution Processing to Organic Solids

Debashish Mukherji ^{1,*}  and Kurt Kremer ² ¹ Quantum Matter Institute, University of British Columbia, Vancouver, BC V6T 1Z4, Canada² Max Planck Institute for Polymer Research, Ackermannweg 10, 55128 Mainz, Germany; k.kremer@mpip-mainz.mpg.de

* Correspondence: debashish.mukherji@ubc.ca

Abstract: Polymeric materials are ubiquitous in our everyday life, where they find a broad range of uses—spanning across common household items to advanced materials for modern technologies. In the context of the latter, so called “smart polymers” have received a lot of attention. These systems are soluble in water below their lower critical solution temperature T_ℓ and often exhibit counterintuitive solvation behavior in mixed solvents. A polymer is known as smart-responsive when a slight change in external stimuli can significantly change its structure, function and stability. The interplay of different interactions, especially hydrogen bonds, can also be used for the design of lightweight high-performance organic solids with tunable properties. Here, a general scheme for establishing a structure–property relationship is a challenge using the conventional simulation techniques and also in standard experiments. From the theoretical side, a broad range of all-atom, multiscale, generic, and analytical techniques have been developed linking monomer level interaction details with macroscopic material properties. In this review, we briefly summarize the recent developments in the field of smart polymers, together with complementary experiments. For this purpose, we will specifically discuss the following: (1) the solution processing of responsive polymers and (2) their use in organic solids, with a goal to provide a microscopic understanding that may be used as a guiding tool for future experiments and/or simulations regarding designing advanced functional materials.

Keywords: polymer solution; smart polymers; coil–globule transition; solvent mixtures; organic solids; thermal conductivity



Citation: Mukherji, D.; Kremer, K. Smart Polymers for Soft Materials: From Solution Processing to Organic Solids. *Polymers* **2023**, *15*, 3229. <https://doi.org/10.3390/polym15153229>

Academic Editors: Amitesh Maiti, Ying Li and Andrew P. Saab

Received: 5 July 2023
Revised: 26 July 2023
Accepted: 27 July 2023
Published: 29 July 2023



Copyright: © 2023 by the authors. Licensee MDPI, Basel, Switzerland. This article is an open access article distributed under the terms and conditions of the Creative Commons Attribution (CC BY) license (<https://creativecommons.org/licenses/by/4.0/>).

1. Overview

Just over a century ago, Hermann Staudinger, in a pioneering work, proposed how small molecules can join hands to form covalently connected long macromolecules, and this led to the foundation of modern synthetic polymer science [1]. Ever since this early discovery, the field of polymer science has come a long way, where various complex structures have been proposed for their use in designing high-performance functional materials for various desired applications [2–11]. Polymers are of particular interest, because they provide the basic building blocks for many modern materials of our daily life. This is particularly because polymers are a class of soft matter, where their relevant energy scale is of the order of $k_B T$ (at room temperature) [12–14], with k_B being the Boltzmann constant, and, thus, they are dictated by large conformational and compositional fluctuations. This makes the processes of entropy as important as those of energy, and the microscopic understanding of this entropy–energy balance is at the heart of all soft materials design.

Traditionally, most commonly used polymers have included those that are dominated by van der Waals (vdW) interactions; examples include, but are not limited to, polystyrene (PS), polyethylene (PE), polypropylene (PP), poly(N-acryloyl piperidine) (PAP), and poly(methyl methacrylate) (PMMA). Recent interests have been diverted towards bio-compatible and thermoresponsive polymer architectures, which are often also referred to

as “smart” polymers [15–19]. Some of the common examples of smart polymers include poly(acrylic acid) (PAA), polyacrylamide (PAM), poly(*N*-isopropyl acrylamide) (PNIPAM), and poly(vinyl alcohol) (PVA). Because of the hydrogen bond (H-bond) nature of the inter- and intramolecular interactions, the strength of which is between $4\text{--}8 k_B T$ [20], these systems are soluble in water when the temperature T is lower than the “so called” lower critical solution temperature (LCST) T_ℓ . For $T > T_\ell$, a chain undergoes a coil-to-globule transition [5,18,21–24]. This is because the increase in T breaks a fraction of polymer–water H-bonds, which thus also destroys the water caging around a polymer, which is responsible for keeping a chain expanded in water. In this process, the expelled water molecules, from within the first solvation shell of a polymer chain, gain translational entropy that is larger than the conformational entropy loss upon collapse, thereby making the LCST an entropy-driven process [12–14]. In the microgel community, T_ℓ is commonly known as the volume phase transition temperature T_{VPTT} [25–27]. On the contrary, when a chain expands upon an increase in T , it is known as the upper critical solution temperature T_u and is driven by energy. In Figure 1, we show the generic phase diagrams of polymer solutions with a UCST (part a) and an LCST (part b). Note that unless stated otherwise, we will primarily focus on LCST polymers in this review.

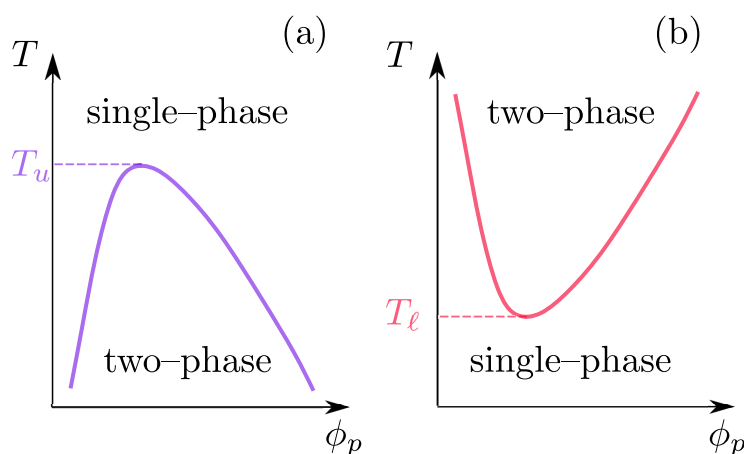


Figure 1. A simple schematic representation of the phase behavior of polymer solutions. Parts (a,b) show the upper critical (UCST) and the lower critical (LCST) solution temperature behaviors, respectively. Here, ϕ_p is the polymer volume fraction, T_u is the UCST, and T_ℓ is the LCST.

Starting from a good solvent condition in an LCST collapse (i.e., for $T < T_\ell$), increasing the effective attraction between monomers causes the polymer to eventually collapse into a globule in the case of isolated chains (or phase separation in solutions). This globular state is dictated by balancing the attractive second virial contributions $-|\mathcal{V}|$ and the three-body repulsion [12–14], where \mathcal{V} is the monomer-excluded volume. Here, a conventional Θ collapse of a polymer is characterized as a second-order phase transition, where the Θ point (or the critical point) is dictated by the large diverging fluctuations. However, there are also many cases where hysteresis is observed near T_ℓ [21,28,29], which is a typical indication of a first-order transition [30,31]. In the case of LCST polymers, first-order [21,28,29], as well as second-order [22] behavior, can be observed.

The most commonly known examples of LCST polymers are poly(ethylene oxide) (PEO) and/or poly(*N*-isopropyl acrylamide) (PNIPAM) in aqueous solutions. While PEO has a T_ℓ that is almost close to the boiling temperature of water [32–34], PNIPAM has $T_\ell \simeq 305$ K [5,21,23], i.e., a temperature just below the human body temperature. This makes PNIPAM a very interesting and a widely studied polymer. It is also noteworthy that the actual value of T_ℓ of a homopolymer can be significantly tuned through a slight change in the monomeric chemical structures [24]; see Figure 2. Typically, increasing the size of the hydrophobic side group reduces the T_ℓ . However, one special system is poly(*N*-isopropyl methacrylamide) (PNIPMAM), where an additional methyl group attached to the backbone of the PNIPAM increases the T_ℓ to about 313 K for the PNIPMAM in comparison to the

$T_\ell \simeq 305$ K for the PNIPAM [35]. At first sight, this is, at least, counterintuitive and still not readily understood. However, one possible scenario might be that the local chain conformation of the PNIPMAM becomes affected by this methyl side group and effectively reduces the hydrophobic surface area of the chains.

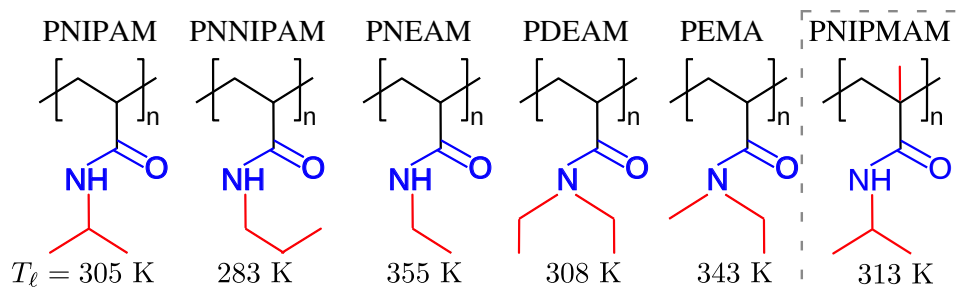


Figure 2. Schematic representation of different homopolymer monomer structures with slight changes in their hydrophobic side groups (represented by red). One special case of poly(*N*-isopropyl methacrylamide) (PNIPMAM) is also shown (within the dashed gray box) that has almost the same chemical structure as poly(*N*-isopropyl acrylamide) (PNIPAM), with an additional a methyl group attached to the backbone; see the text for more details. The corresponding values of the lower critical solution temperature T_ℓ are also highlighted.

Tuning the T_ℓ can not only be obtained in the homopolymer structures, but instead through a possibly better and more versatile protocol, which is to use the copolymer sequences that might provide a greater control on the tunability of the T_ℓ [16,22,24,36–40]. A common technique to increase the T_ℓ is the introduction of more hydrophilic monomers along a polymer backbone [22,23,41,42], while the T_ℓ can be reduced by introducing hydrophobic monomers [22,42]. Here, however, in most cases the interaction of the solvent molecules with one monomer type becomes greatly affected by the solvation structures of the neighboring monomers. This induces a strong crosscorrelation between the different monomer species and, thus, the shift in the T_ℓ remains rather unpredictable (nonlinear) [23,41,42].

A recent experimental study proposed a set of copolymers consisting of ethylene oxide and methylene units, where a linear variation in the cloud point temperature T_{cloud} was observed with the change in the relative variation in monomer concentrations [22,43]. The chemical structure and the variation in the T_{cloud} are shown in Figure 3. The predictability of the T_{cloud} (or T_ℓ) comes from the linear variation in the T_{cloud} ; see Figure 3c. For example, if one requires a particular value of T_{cloud} , data such as the ones from Figure 3c can be used to estimate what relative fraction of ethylene oxide and methylene is needed. The added advantage of this system is that the monomers are connected by the acetal links and, thus, are commonly referred to as polyacetals; see Figure 3a [22]. While polyacetals are LCST thermoresponsive, they are also biodegradable because of their acetal linkage.

The above experiments are very important to provide a guiding path, but the range of the relative monomeric compositions investigated in Ref. [22] remains rather limited because of the synthesis-related limitations. Therefore, simulations (especially the multiscale approaches) may provide a better platform to explore a large range of copolymer configurations with minimalistic computational costs. In this context, a segment-based (i.e., monomer level) coarse-grained (CG) model was developed to investigate the conformational behavior of a broad range of polyacetals [43]; see Figure 4. This structure-based CG model was derived using a combination of the iterative Boltzmann inversion [44,45] and the coordination IBI [46]. Furthermore, this approach makes use of the linear variation of the T_{cloud} with the sequence length (shown in Figure 3c), which highlight that there is no crosscorrelation between the solvation structures of the two monomer species constituting a polyacetal. Therefore, intermolecular CG potentials were derived at the monomer level (shown in Figure 4d), and their derivations were sufficient to explore the conformational behavior of a large set of polyacetal sequences; see Figure 4e–g. Additionally, other than

the consistency with the existing experimental data (highlighted by the cyan oblique circles in Figure 4e–g) [22], this model also found very interesting copolymer structures based on their relative sequences; see the simulation snapshots in Figure 4. We also note in passing that, for the other sequences, such as the nonblock random sequences, the above mentioned CG protocol might need some more fine-tuning.

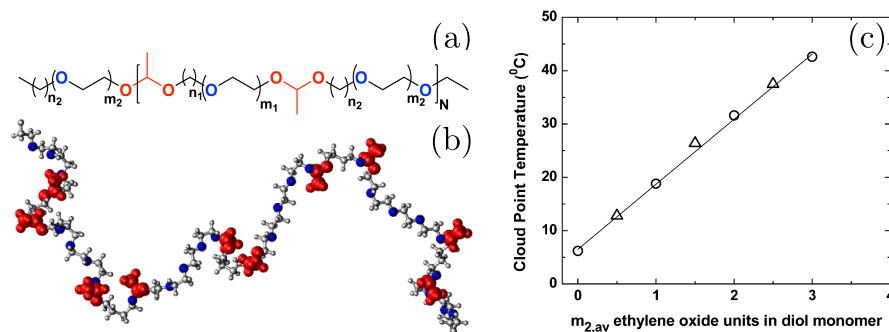


Figure 3. Parts (a,b) show the schematic of an experimentally synthesized polyacetal chain [22] and the corresponding simulation snapshot at 290 K [43], respectively. The number of hydrophobic n_1 and hydrophilic m_i units were tuned to obtain the desired cloud point temperature T_{cloud} . The acetal linkers are represented in red. Part (c) shows the change in T_{cloud} as a function of m_2 . Parts (a,b) have been reproduced with permission from the American Institute of Physics [43], and part (c) has been reproduced with permission from the American Chemical Society [22].

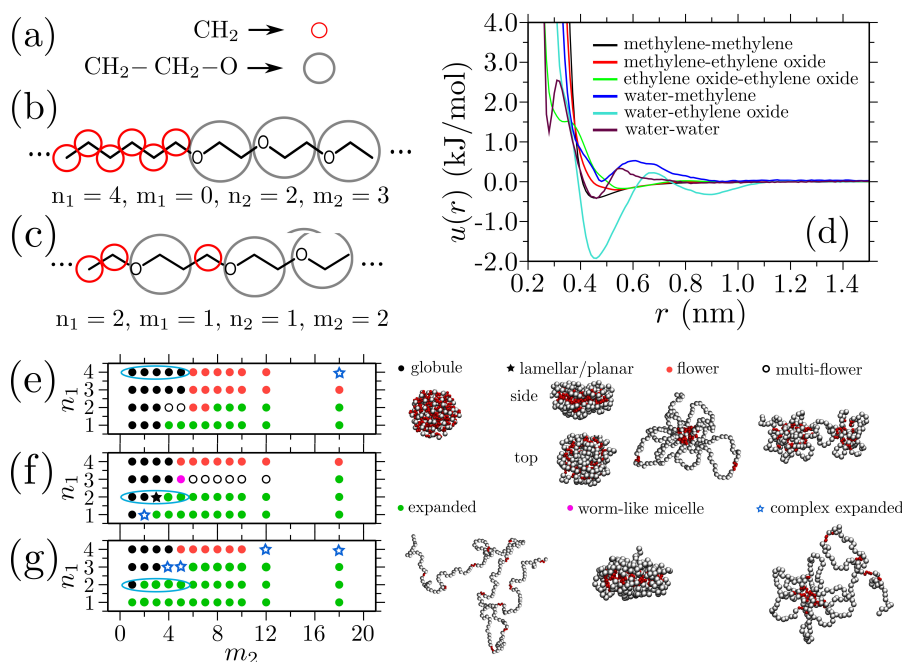


Figure 4. Parts (a–c) show the mapping scheme and the corresponding coarse-grained (CG) representations of two polyacetal chains with different amphiphilic sequences. Part (d) shows the sequence-transferable CG potentials between different pairs. Finally, parts (e–g) show the phase diagrams of 144 chains with different sequences and their corresponding configurations. This figure has been reproduced with permission from the American Institute of Physics [43].

The discussions presented above deal with a reasonably broad range of standard polymer architectures. In addition to these, another set of architectures includes the peptide-based systems that can also mimic the LCST-type phase behavior [15,47]. A common example of peptide-based systems are the elastin-like polypeptides (ELP), which are characterized by the standard sequence (VPGXG) $_n$. Here, V, P, and G are valine, proline, and glycine, respectively. The residue X can be anything but proline. The T_ℓ of an ELP

sequence can be easily tuned by taking an appropriate X [48–50]. Another advantage of ELPs is that the T_ℓ can be further tuned by proline isomerization [51,52], where *cis* and *trans* configurations can significantly alter the water caging around the ELP, which consequently changes its T_ℓ .

While the conformational tuning by changing T yields a flexible route for the solution processing of “smart” polymers and ELPs, it often requires an unusual variation in T and, thus, poses a challenge for the practical use of these polymers. Therefore, a possible alternative might be to use cosolvents as an external stimulus at a fixed T . In this context, it has been well known that the structure, function, and stability of a polymer in water become severely affected by the presence of small molecules [53–70] and/or ions [17,71,72] within the first solvation shell.

The importance of polymer processing in mixed solvents was already highlighted over half a century ago [73–75]. Here, polymer solvation in binary mixtures often appears paradoxical, where a delicate balance of the microscopic interactions between different solution components dictates the macroscopic conformational behavior. Two such phenomena are *co-nonsolvency* and *cosolvency*. Therefore, in the following, we will now focus on polymer solvation in binary mixtures by reviewing two symmetric effects and their thermodynamic origins within the context of multiscale simulations.

2. Co-Nonsolvency

Co-nonsolvency is a generic name given to the phenomenon of polymer collapse in the mixtures of two miscible good solvents. This phenomenon was initially reported for PS solvation in the mixtures of cyclohexane and N,N-dimethylformamide (DMF) [75], where the name co-nonsolvency was initially coined. Even though this phenomenon was discovered for a UCST polymer, it gained popularity in the context of PNIPAM solvation in aqueous alcohol mixtures [53,54]. PNIPAM is a “well known” thermoresponsive polymer that shows LCST phase behavior in pure water. In aqueous alcohol mixtures, the T_ℓ of a PNIPAM system first decreases with the increasing alcohol (or cosolvent) mole fraction x_c and again increases sharply around $x_c \simeq 0.40$; see Figure 5a. More specifically, when a small amount of alcohol is added in water at a fixed T (for example at $T = 300$ K), a PNIPAM chain collapses and then again opens up when $x_c \geq 0.40$ [55,76]; see Figure 5b.

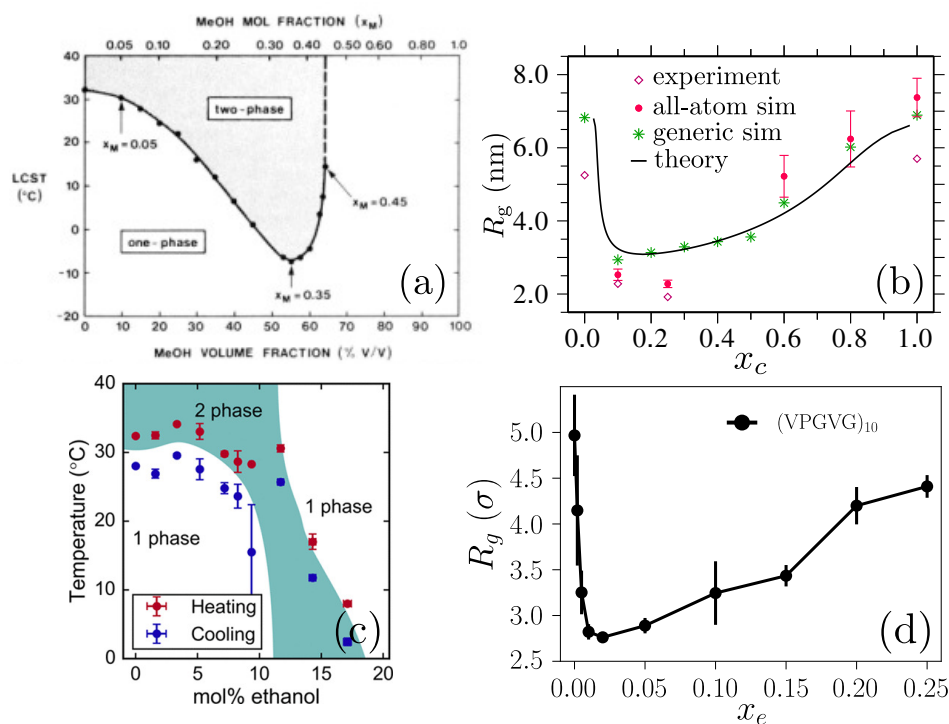


Figure 5. The phase diagrams for a poly(N-isopropyl acrylamide) (PNIPAM) [54]: (part (a)) and an

elastin-like polypeptide (ELP) [77] (part (c)) in aqueous alcohol mixtures. The corresponding single-chain gyration radii R_g for PNIPAM (part (b)) and ELP (part (d)) are also shown. While R_g calculated from the different techniques are shown for PNIPAM [76] in panel (b), ELP data were calculated using generic simulations [78]. Figures in parts (a,c,d) have been reproduced with permission from the American Chemical Society [54,77,78] and part (b) has been reproduced with permission from the Royal Society of Chemistry [76].

It is not only that the PS and PNIPAM show co-nonsolvency-like phase behavior. A rather broad range of polymers shows similar solvation behavior in their respective binary solutions [56,57,79–83]. This list also includes standard ELPs; see Figure 5c,d for the phase behavior obtained in experiments [77] and the corresponding conformational transition from a generic simulation model [78]. One special case, however, is PDEAM in aqueous–alcohol mixtures; see the chemical structure in Figure 2. It was shown that PDEAM does not show co-nonsolvency in aqueous methanol [84], but it collapses in aqueous ethanol [82]. We also wish to point out that the range of co-nonsolvency collapse is a T , molecular weight M_w , and cosolvent-dependent quantity [85–87].

If two solvents are good for a polymer and also remain fairly miscible, why should a polymer collapse within certain combinations of such mixed solvents? In recent times, there has been considerable interest to investigate the phenomenon of co-nonsolvency using a broad range of experimental, computational, and theoretical techniques. In particular, analytical and simulation efforts have been devoted to unveiling the microscopic origin of co-nonsolvency, where three main mechanisms have been proposed, namely, the Flory–Huggins mean field description [53], the cooperativity effect [58,85], and preferential binding [63,88], which we will now review in the context of their complementary experiments.

2.1. Flory–Huggins Mean Field Description

A standard mean field thermodynamic description of polymer conformation is the Flory–Huggins (FH) theory [12–14]. Here, when a polymer p with a chain length N_l at a volume fraction ϕ_p is dissolved in a binary mixture of the solvent s and cosolvent c , the free energy \mathcal{F}_{FH} is written as follows [12–14]:

$$\begin{aligned} \frac{\mathcal{F}_{\text{FH}}}{\kappa_B T} = & \frac{\phi_p}{N_l} \ln \phi_p + x_c(1 - \phi_p) \ln [x_c(1 - \phi_p)] \\ & + (1 - x_c)(1 - \phi_p) \ln [(1 - x_c)(1 - \phi_p)] \\ & + \chi_{ps} \phi_p(1 - x_c)(1 - \phi_p) \\ & + \chi_{pc} \phi_p x_c(1 - \phi_p) \\ & + \chi_{sc} x_c(1 - x_c)(1 - \phi_p)^2. \end{aligned} \quad (1)$$

The first three and the last three terms represent the mixing entropy and the interaction between different solution components, respectively. χ_{ij} is the interaction parameter between the components i and j . The second-order expansion of Equation (1) yields the estimate of the polymer-excluded volume \mathcal{V} (or the second virial):

$$\mathcal{V} = 1 - 2(1 - x_c)\chi_{ps} - 2x_c\chi_{pc} + 2x_c(1 - x_c)\chi_{sc}. \quad (2)$$

Furthermore, $\mathcal{V} = -2\pi \int [e^{-v(r)/k_B T} - 1] r^2 dr$ gives a direct indication of the solvent quality via the effective monomer–monomer interaction $v(r)$. For example, in a good solvent condition, $\mathcal{V} > 0$, where the single-chain structure factor follows a scaling relation $S(q) \sim q^{-5/3}$. Increasing the monomer–monomer attraction brings a polymer into the Θ condition, where $\mathcal{V} = 0$, and $S(q) \sim q^{-2}$. A further increase in the monomer–monomer attractions the takes a system to the globular state, where $\mathcal{V} < 0$, and $S(q) \sim q^{-4}$ [12–14].

The description in Equation (1) suggests that $\chi_{ij} < 1/2$ for a good solvent polymer solution [12–14]. Furthermore, when two cosolvents are perfectly miscible (i.e., $\chi_{sc} = 0$), the first two terms of Equation (2) yield a linear variation in \mathcal{V} with x_c ; see the blue line in Figure 6a. Only when $\chi_{sc} < 0$ can co-nonsolvency be observed (i.e., $\mathcal{V} < 0$); see the red line in Figure 6a.

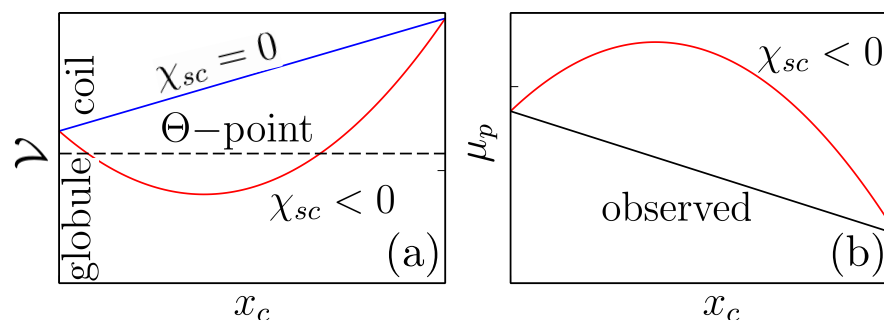


Figure 6. A schematic representation of the polymer-excluded volume \mathcal{V} (part (a)) and chemical potential μ_p (part (b)) as a function of cosolvent mole fraction x_c . The curves are shown for different solvent–cosolvent interactions χ_{sc} . The Θ point corresponds to $\mathcal{V} = 0$. This figure has been reproduced with permission from the American Institute of Physics [89].

Under the infinite dilution limit of a polymer (i.e., $\phi_p \rightarrow 0$), Equation (1) also gives an estimate of the polymer chemical potential μ_p :

$$\begin{aligned} \bar{\mu}_p(\phi_p \rightarrow 0) &= \left. \frac{\partial \mathcal{F}_{\text{FH}}}{\partial \phi_p} \right|_{\phi_p \rightarrow 0} \\ &= \text{const} - x_c \ln x_c - (1 - x_c) \ln(1 - x_c) \\ &\quad + (1 - x_c)\chi_{ps} + x_c\chi_{pc} - 2x_c(1 - x_c)\chi_{sc}. \end{aligned} \quad (3)$$

When $\chi_{sc} < 0$, Equation (3) yields the expected variation shown by the red line in Figure 6b, i.e., it becomes energetically expensive to solvate a polymer within the intermediate range of x_c where a polymer collapses. As we will show in Section 2.3, the observed trend in μ_p , represented by the black line in Figure 6b, requires an unrealistic cost of driving the bulk binary mixture to phase separation by using $\chi_{sc} \gg 0$.

Note that when the solvent–cosolvent interaction becomes attractive (i.e., $\chi_{sc} < 0$), it is quite obvious why a polymer falls out of the solution [53,65,90]. However, it is readily known that the common solvent mixtures where co-nonsolvency is observed, such as the water–alcohol mixtures, both (co)solvents are typically only fairly miscible, i.e., $\chi_{sc} \simeq 0$. Indeed, the experimental [91,92] and the simulation [27,93] data for aqueous alcohol mixtures are in agreement with this argument. Therefore, it is not quite obvious how the standard FH-based mean field theory can lead to the phenomenon of co-nonsolvency. However, it has been discussed that, if the three-body interactions are considered, co-nonsolvency can be observed within the mean field description [94,95].

2.2. Cooperativity Effect

An alternative theoretical approach to describe the co-nonsolvency phenomenon is the cooperativity effect [58,85]. This approach was predominantly developed for PNIPAM and described its LCST response [96]. This approach considers the following phenomena: (i) the formation an H–bond between one water molecule and a monomer, which cooperatively facilitates the formation of the next H–bonds. (ii) The backbone segments that are not bound to the water aggregate into a collapsed region. This model was then extended to describe the co-nonsolvency phenomenon where both water molecules and alcohols were treated equally, therein estimating the interaction parameters accounting for different affinities and cooperativity effects. This approach used a set of parameters that could very well describe

the experimental results of PNIPAM solvation in water–methanol mixtures [58] or some mixed solvents in general [66,85,97].

2.3. Preferential Interactions

Another approach to describe the phenomenon of co-nonsolvency uses the idea of preferential polymer–cosolvent binding with respect to the solvent–polymer interactions. As seen from the all-atom simulations in Figure 7a, there is an excess of cosolvents within the first solvation shell of a PNIPAM chain, i.e., when $x_c^* > 1$ for $r \leq 0.6$ nm [98]. More specifically, when a small amount of cosolvent molecules is added in a polymer–solvent solution, they cluster around the monomers because of their preferential binding and promote the aggregation of monomers to minimize the binding free energy. In this process, cosolvent molecules form sticky contacts between monomers that are topologically far along a chain backbone that is facilitated by the formation of segmental loops; see the inset in Figure 7a [88].

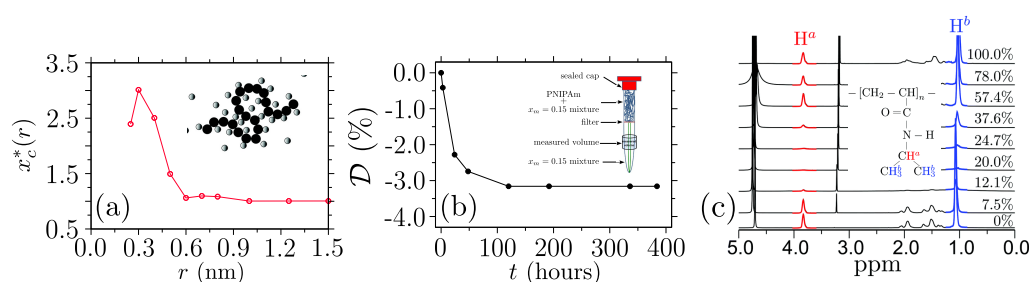


Figure 7. Part (a) shows the normalized methanol mole fraction $x_c^* = x_c(r)/x_c$ as a function of the radial distance r from a poly(N-isopropylacrylamide) (PNIPAM) backbone. In a nutshell, an excess occurs when $x_c^* > 1$, and $x_c^* = 1$ represents the bulk mixing ratio x_c . This dataset is shown for $x_c = 0.1$. In the inset of part (a), a schematic of polymer (black circles) is shown in the presence of cosolvent molecules (gray circles). Part (b) shows the percentage of excess methanol molecules absorbed by the PNIPAM sample in the upper part of the nuclear magnetic resonance (NMR) measurement tube (see the inset). A depletion of methanol content in the lower compartment of the NMR tube gives a direct estimate of the methanol intake in the PNIPAM. The data is shown for $x_c = 0.15$. Finally, part (c) presents the proton NMR spectra of the hydrogen atoms (highlighted in the inset) as a function of x_c . Reduced intensity is a measure of the dynamics of the PNIPAM side group. These figures have been reproduced with permission from the Royal Society of Chemistry [76].

Within a simple scaling argument, formation of a loop of segment length n can be characterized by the free energy difference $\Delta\mathcal{F}(n)$ to form a loop from an extended conformation. Here, the partition function of an expanded chain of length N_ℓ and with an end-to-end distance R_{ee} can be defined as follows [14]:

$$Z(R_{ee}) \propto Q^{N_\ell} N_\ell^{\gamma-1}, \quad (4)$$

and for the case when $R_{ee} \rightarrow 0$,

$$Z(R_{ee} \rightarrow 0) \propto Q^{N_\ell} N_\ell^{\alpha-2}. \quad (5)$$

The $1/Q$ value is the critical fugacity, and $\gamma = 1.15$ and $\alpha = 0.2$ are the critical exponents [12–14]. Following these definitions, one can estimate $\Delta\mathcal{F}(n) = mk_B T \ln(n)$ with $m = 1.95$. This estimate suggests that the energy penalty to form a short segmental loop is of the order of a few $k_B T$ [88,89].

The preferential binding picture is supported by the proton NMR experiments [76]. For example, as measured by the depletion \mathcal{D} of cosolvent molecules in the lower compartment of an NMR tube (see Figure 7b), the same amount of cosolvents were absorbed by the PNIPAM sample in the upper compartment of the NMR tube; see the inset of Figure 7b.

Note that the sealed top cap prevented the evaporation of methanol molecules, as also shown by the plateau in Figure 7b for $t > 150$ h.

The excess of cosolvent molecules populated the side groups of the PNIPAM. Something that speaks in this favor is that the side groups of the PNIPAM became more rigid within the range of $10\% \leq x_c \leq 40\%$, i.e., when a PNIPAM collapsed. Furthermore, the side groups organized in such a way that they were buried inside a collapsed PNIPAM, encapsulated by a certain amount of methanol molecules, and, thus, formed a fluffy PNIPAM globule [76]. Note that this was a different outcome from the standard picture of polymer collapse in poor solvents, which will be discussed in detail at a later stage in this review. The solvation of PNIPAM in aqueous urea mixtures also shows a similar preferential binding trend. In this context, it has been shown that a PNIPAM chain collapses in aqueous urea by forming H-bonded bridging urea molecules that bind to two monomers far along a chain backbone [17,67].

Note also that earlier studies have highlighted the importance of preferential binding to describe polymer solvation in binary mixtures [74,99,100]. A recent work also emphasized that the preferential binding may not be a prerequisite for co-nonsolvency [101], which may, however, require strong solvent–cosolvent interactions.

The above discussions focused on describing general polymer conformations (i.e., going from a random coil to a collapsed globule) without specifically ordered regions. However, cosolvent effects are also most commonly associated with the ability of proteins and polypeptide sequences to form well-defined secondary structures [102–109]. In this context, urea is a common osmolyte that is known to denature native protein structures via preferential binding [103–106,108,109]. On the contrary, studies have also indicated that a certain set of polypeptides (such as polyalanine or alanine-rich sequences) may show the signatures of folding in aqueous urea mixtures [102,107,110]. It can be appreciated from the snapshots of Figure 8 that a polyalanine remains in a rather globular conformation in pure water (part a), and a well-defined secondary structure can be observed in 4 M aqueous urea mixtures (part b). Furthermore, simulation results have suggested that the preferential binding alone cannot account for this behavior; rather, a delicate balance between the preferential peptide–urea H-bond and the dipole–dipole interactions (DDIs) controls the conformational transition of polyalanines in aqueous urea mixtures [110]. This interpretation is of particular importance, because DDIs are known to play a key role in protein solvation, as highlighted in a recent experimental study [111], yet they are poorly investigated in the existing literature.

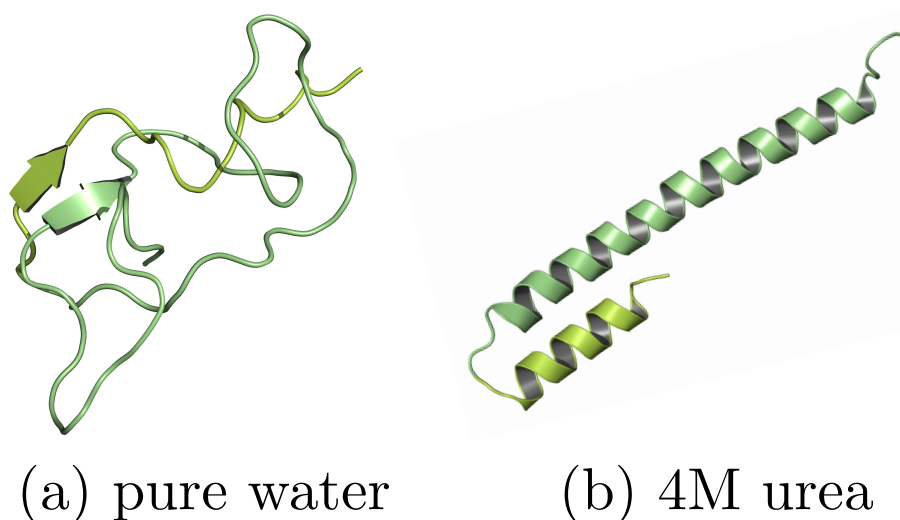


Figure 8. Simulation snapshots showing the secondary structure of a polyalanine in pure water (part (a)) and in 4 M aqueous urea mixture (part (b)). A clear indication of stable secondary structure is shown in 4 M aqueous urea mixtures. This figure has been reproduced with permission from the American Chemical Society [110].

2.3.1. Solvation Thermodynamics: Kirkwood–Buff Theory of Solution

Polymer–cosolvent preferential binding can also result in an interesting thermodynamic trend, as estimated by the variation in the polymer chemical potential μ_p with x_c . A direct method to calculate μ_p is the fluctuation theory of Kirkwood and Buff (KB). The KB theory is an extremely powerful tool to calculate the solvation properties of complex multicomponent mixtures, and it has been extensively used in studying solvent mixtures [91,112–114], polymer solutions [63,115], ionic systems [116,117], and/or long-chain polymer blends [118,119].

In a nutshell, the KB theory connects the fluctuations in a grand canonical ensemble (i.e., a constant solution chemical potential μ , constant volume V , and constant T ensemble) to pair distribution functions $g_{ij}^{\mu VT}(r)$ via the “so called” Kirkwood–Buff integral (KBI) [91,112]:

$$G_{ij} = 4\pi \int_0^\infty [g_{ij}^{\mu VT}(r) - 1] r^2 dr = V \left[\frac{\langle N_i N_j \rangle - \langle N_i \rangle \langle N_j \rangle}{\langle N_i \rangle \langle N_j \rangle} - \frac{\delta_{ij}}{\langle N_j \rangle} \right]. \quad (6)$$

Here, G_{ij} is known as the excess coordination between two different species i and j that are blended in at different x_j . In polymer physics, $\mathcal{V}_{ij} = -G_{ij}/2$ gives an estimate of the monomer-excluded volume. The thermal averages are denoted by brackets $\langle \cdot \rangle$. N_i is the number of particles of species i , and δ_{ij} is the Kronecker delta. To precisely calculate G_{ij} , the correlations have to be integrated to $r \rightarrow \infty$. However, within the mid-sized and closed boundary simulation setups [112], G_{ij} is usually calculated from the r values that are slightly larger than the typical correlation lengths $r_{\text{corr}} > 1.5$ nm in the aqueous systems. We also note in passing that there are several more sophisticated simulation protocols that usually deal with semigrand canonical schemes [63,120] or by using fluctuations [114,121,122].

Within the framework of KB theory, μ_p can be calculated using the following formula [63,91,123]:

$$\lim_{\phi_p \rightarrow 0} \frac{\partial \mu_p}{\partial x_c} = \frac{k_B T (G_{ps} - G_{pc})}{1 - \rho_c (G_{sc} - G_{cc})}, \quad (7)$$

with ρ_c being the number density of the cosolvents. Figure 9 shows the shift in μ_p as a function of x_c .

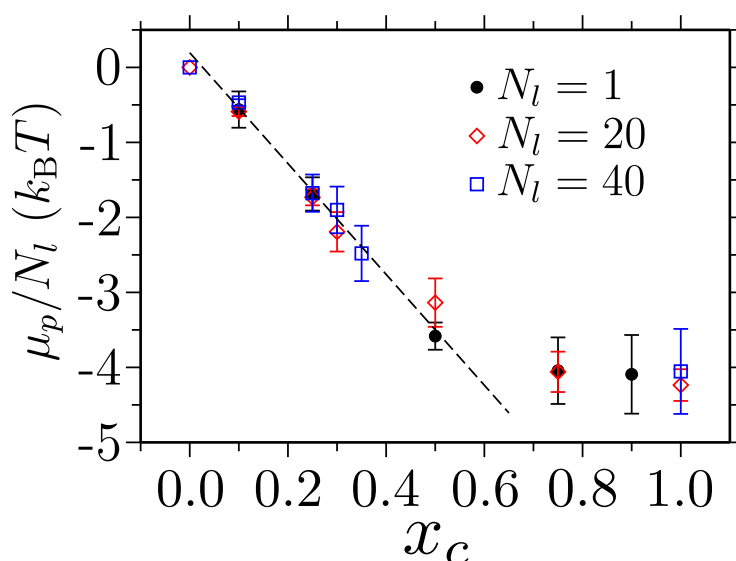


Figure 9. The shift in polymer chemical potential μ_p per monomer as a function of methanol mole fraction x_c . Data are shown for a poly(*N*-isopropyl acrylamide) (PNIPAM) in water–methanol mixtures with three different chain lengths N_l at a temperature $T = 300$ K. This figure has been reproduced with permission from the American Chemical Society [63].

It can be appreciated that, upon adding cosolvent molecules (in this case, methanol) in aqueous–PNIPAM solutions, the solvent quality becomes better and better [63]. Furthermore, data have also revealed that, in this case, there was a contrast of about $4k_B T$ between the solvent–polymer and the cosolvent–polymer interactions; thus, the cosolvent molecules were a significantly better good solvent for the polymer than the solvent molecules [63,88].

The behavior observed in Figure 9 is different from what would be expected from the mean field description of polymer solutions; see the red dataset in Figure 6b, i.e., when a polymer collapses, it should become energetically costlier to solvate. This stark qualitative difference suggests that the polymer conformation and its thermodynamic state are not connected in the conventional way, thus presenting a need for an analytical treatment that goes beyond the standard Flory–Huggins mean field description [53,89].

We also highlight that the shift in μ_p (observed in Figure 9) can be used to develop thermodynamically consistent generic models. This can be achieved by simply treating the interparticle interactions based purely on the Lennard–Jones potential and then tuning the relative parameters between different solution components that reproduce the reference all-atom μ_p . This approach can reasonably capture the solvation behaviors of PNIPAMs [88] and ELPs [78] in aqueous–alcohol mixtures.

2.3.2. Competitive Displacement of Solvents by Cosolvents

It has been demonstrated that co-nonsolvency has been observed for a broad range of chemical specific systems [53,54,56,57,77,80–82], which thus suggests that there may be a more generic microscopic picture of this complex solvation behavior. In this context, a simple generic picture was proposed that made use of the idea of preferential cosolvent–monomer interactions, as shown in Figures 7 and 9. This treatment considers a polymer as a surface with \mathcal{N} adsorbing sites, where both solvents and cosolvents compete to be adsorbed, as described within the Langmuir-like adsorption isotherm [124]. This is in contrast to the mean field picture of polymer solution, where the (co)solvents effects are treated as the average field, irrespective of their spatial distributions around a polymer.

When a polymer collapses under the influence of a cosolvent, a collapsed globule contains a large fraction of cosolvent molecules that bind to more than one monomer to form a sticky bridging contact; see the schematic in the inset of Figure 7a. Note that a cosolvent molecule is considered to be confined by the local polymer environment when its residence time is longer than the time it takes for the polymer to move its own size. In this case, a polymer globule contains a fraction of bridging cosolvents ϕ_B , a fraction of cosolvents that are adsorbed on a single site ϕ , and the remaining $1 - \phi_B - \phi$ sites are occupied by the solvent molecules. As expected, the ϕ_B bridging cosolvents show a hump within the range of x_c when a polymer collapses; see the simulation data in Figure 10a. Here, the individual bridging contacts consist of a few cosolvent molecules, and this is not only by one cosolvent [88].

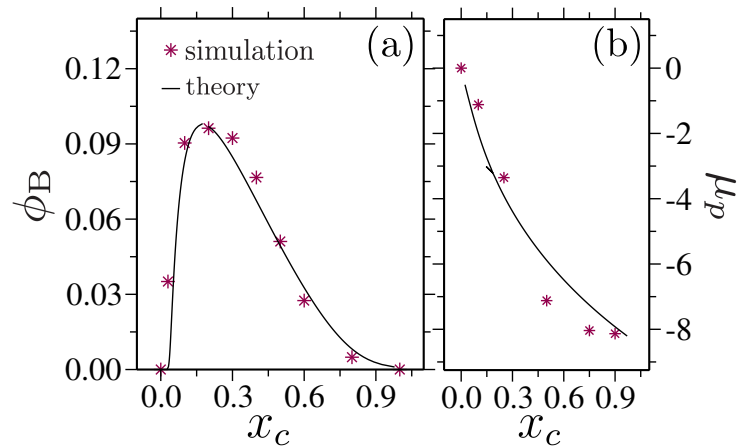


Figure 10. Part (a) shows the fraction of bridging cosolvents ϕ_B as a function of cosolvent mole fraction x_c . ϕ_B forms sticky contacts between two monomers topologically far along the chain contour. Part (b) shows the shift in polymer chemical potential $\bar{\mu}_p$ as a function of x_c . The lines are the results of obtained from the analytical model in Equations (9) and (10). Datasets have been taken from Refs. [88,89].

Within the adsorption isotherm picture, the free energy per site Ψ can then be written as follows:

$$\begin{aligned} \frac{\Psi}{\kappa_B T} &= \phi \ln(\phi) + 2\phi_B \ln(2\phi_B) \\ &+ (1 - \phi - 2\phi_B) \ln(1 - \phi - 2\phi_B) \\ &- \mathcal{E}\phi - \mathcal{E}_B\phi_B - \frac{\mu}{\kappa_B T}(\phi + \phi_B). \end{aligned} \tag{8}$$

The first three terms are the mixing entropic contributions, and the factor of two represents the simple picture that a collection of bridging cosolvents bind to two monomers. The next two terms are related to the adsorption energies of the bridging \mathcal{E}_B and single site \mathcal{E} cosolvent molecules. $\mu = k_B T \ln(x_c)$ is the cosolvent chemical potential in the bulk solution at x_c . Furthermore, $\mathcal{E}_B = 2\mathcal{E} - mk_B T \ln(n)$, i.e., \mathcal{E}_B is reduced with respect to $2\mathcal{E}$ by the cost of forming a loop of the segmental length n , which was discussed earlier in this review. By minimally mixing Equation (8) one obtains the following:

$$\begin{aligned} 16\phi_B^2 x_c &= x_c^a \left\{ \left(\frac{x_c^a}{x_c^b} \right)^{1/2} \phi_B^{m/2} (1 - 2\phi_B) \right. \\ &\left. \pm \sqrt{\left(\frac{x_c^a}{x_c^b} \right) \phi_B^m (1 - 2\phi_B)^2 - 16\phi_B^2} \right\}^2, \end{aligned} \tag{9}$$

where $x_c^a = e^{-\mathcal{E}}$, and $x_c^b = e^{-2\mathcal{E}}$. The solution of Equation (9) is drawn by the solid line in Figure 10a, together with the ϕ_B calculated directly from the simulations. A reasonable consistency between the simulation and theoretical data was shown to be evident.

The particle-based description can also provide an analytical expression for μ_p , which is expressed as follows:

$$\frac{\mu_p}{\kappa_B T} \propto -m\phi_B \ln \left\{ 1 + \phi_B^{m/2} \left(\frac{x_c}{x_c^b} \right)^{1/2} + \left(\frac{x_c}{x_c^a} \right) \right\}. \tag{10}$$

A good agreement is obtained by simply inserting the values for m in Equation (10); see Figure 10b.

We wish to highlight that a more generalized picture of cosolvent cluster binding was also formulated in [89]. Moreover, we only discuss the simplest picture that can capture

the leading-order contribution to the generic microscopic picture of co-nonsolvency in our review. Note as well that, even when the theoretical framework based on the Langmuir-like adsorption isotherm was initially proposed for polymer solutions [88,89], it was later extended to study the co-nonsolvency behavior of polymer brushes [69,94,95].

3. Cosolvency

In contrast to co-nonsolvency, one also observes the phenomenon that a polymer swells in the mixtures of two poor solvents. This phenomenon is commonly referred to as cosolvency [125], which is typically observed for PMMAs in mixtures of water and short alcohols (such as methanol, ethanol, propanol, and/or isopropanol) [126–128]. PMMAs also show cosolvency in 2-butanol and 1-chlorobutane mixtures [125]. Additionally, poly(N-(6-acetamidopyridin-2-yl)acrylamide) (PNAPAAm) [129] and corn starch [130] also show cosolvency in aqueous alcohol mixtures. For example, when both water and alcohols are poor solvents for PMMAs, the mixture is a somewhat better solvent that attains a maximum around $x_c \simeq 0.7$; see the orange dataset in Figure 11a and the experimental data in Refs. [126–128].

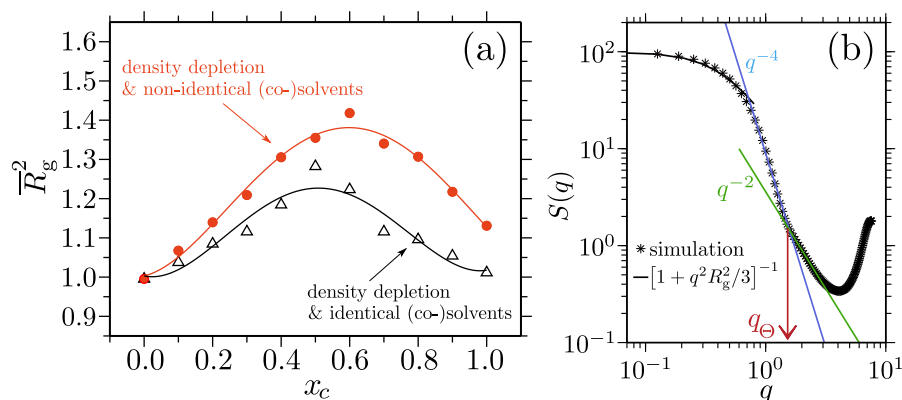


Figure 11. Part (a) shows the normalized squared radius of gyration $\bar{R}_g^2 = \langle R_g^2 \rangle / \langle R_g^2(x_c = 0) \rangle$ as a function of cosolvent mole fraction x_c . Results are shown for the generic simulations and for two different cases described in the legends. $\langle R_g(x_c = 0)^2 \rangle = 2.6 \pm 0.4\sigma^2$ and $\bar{R}_\Theta^2 = 2.13$ with $\bar{R}_\Theta = R_\Theta / R_g(x_c = 0)$ define the normalized Θ -point gyration radius. The orange data set closely mimics PMMA behavior in aqueous alcohol mixtures. Part (b) illustrates single-chain form factor $S(q)$, which shows the conformations for $x_c = 0.0$ and $x_c = 0.7$ in the orange dataset of part (a). The black line represents the Guiner region for $q \rightarrow 0$, and the vertical arrow indicates the effective Θ -like blob size at $q = q_\Theta$. Datasets have been taken from Ref. [131].

In a standard poor solvent (i.e., in contrast to the co-nonsolvency-based collapse described above) the effective attraction between the two monomers of a polymer can be seen as a depletion-induced attraction, which is a phenomenon that is well-known in colloidal science [132–136]. More specifically, monomer–monomer attraction will occur in a system of purely repulsive components if the monomer–solvent repulsion (or excluded volume) becomes larger than the monomer–monomer repulsive interaction. In this case, the resultant single-chain structure in a dilute solution can be well-described by the sphere scattering following $S(q) \propto q^{-4}$ [12–14]. This picture holds for PMMA behavior in pure water or in pure alcohol. However, when a polymer swells within the intermediate solvent–cosolvent mixing ratios, this does not mean that a polymer opens up to a fully expanded coil. Instead, the generic simulation data on cosolvency proposes that, while a chain remains globally collapsed around $x_c \simeq 0.7$ (shown by $S(q) \propto q^{-4}$ in Figure 11b), it consists of Θ blobs with typical sizes of $\ell_\Theta \simeq 4.5\sigma$ for this specific set of parameters (shown by $S(q) \propto q^{-2}$ in Figure 11b) [131].

What causes the swelling of a polymer in mixed poor solvents? This was answered within the framework of depletion-induced attraction [131]. For example, the magnitude of depletion interaction has been directly related to the total ρ of the bulk

solution [132–136]. Therefore, when a polymer swells, there should be some indication via the ρ around $x_c \simeq 0.7$. Indeed, a closer look at the aqueous alcohol mixtures reveals that the ρ shows a dip in ρ [131,137] to attain a minimum around $x_c \simeq 0.5$. The larger the alcohol is, the larger the deviation that is measured from the linear interpolation of the ρ . This deviation is a key factor with respect to swelling a polymer, because the reduction in the ρ also reduces the repulsive forces between a polymer and the bulk solution components. Furthermore, while the identical polymer–solvent and polymer–cosolvent interactions swell a polymer at $x_c \simeq 0.5$ (see the black dataset in Figure 11a), the non-identical interactions lead the solvation peak to shift towards a higher x_c (see the orange dataset in Figure 11a) [131]. In summary, while the pure poor solvent-driven collapse can be viewed as a depletion-induced attraction, the swelling is due to the “depleted depletion” because of the bulk solution behavior.

Flory–Huggins Mean Field Theory

The cosolvency phenomenon is not only an opposite effect to that of the co-nonsolvency phenomenon; it can also be explained within the Flory–Huggins-type mean field description. As discussed in the preceding paragraph, cosolvency naturally emerges at a constant pressure P and is dictated by the dip in the ρ . For this analytical treatment, we consider $\phi_p \rightarrow 0$, and, thus, the majority of the system volume is occupied by solvent–cosolvent mixtures. Therefore, it can be treated within a simplified limit of the binary mixture. In this case, the total free energy can be written as follows [131]:

$$\begin{aligned} \frac{\mathcal{F}}{\kappa_B T} &= \frac{\mathcal{F}_s(v)}{\kappa_B T} \\ &+ x_c \ln(x_c) + (1 - x_c) \ln(1 - x_c) \\ &+ \chi_{sc}(v)x_c(1 - x_c), \end{aligned} \quad (11)$$

where $\mathcal{F}_s(v)$ and $\chi_{sc}(v)$ are the molar volume (v) dependent-free energy of the pure (co)solvent and solvent–cosolvent interaction parameters, respectively. For a given P , v is thus controlled by the following:

$$P = P_s(v) - \kappa_B T x_c (1 - x_c) \frac{\partial \chi_{sc}(v)}{\partial v}, \quad (12)$$

with $P_s(v) = -\partial \mathcal{F}_s / \partial v$ being the pressure of the reference system. For a small variation in v , one obtains $v = v_0[1 + \zeta x_c(1 - x_c)]$, where

$$\zeta = \frac{\kappa_B T}{v} \frac{\partial \chi_{sc}(v)}{\partial v} \left[\frac{\partial P_s(v)}{\partial v} \right]^{-1}, \quad (13)$$

which measures the relative sensitivity of the interaction parameter and reference pressure to v . The change in χ_{sc} between the constant density and the constant pressure ensembles can then be estimated using the following:

$$\begin{aligned} \chi_{sc}(v) &= \chi_{sc}(v_0) \\ &+ v \frac{\partial \chi_{sc}(v)}{\partial v} \Big|_{x_c \rightarrow 0} \zeta x_c (1 - x_c). \end{aligned} \quad (14)$$

Since $v \partial \chi_{sc}(v) / \partial v \sim \zeta$, the χ_{sc} obtained between different ensembles is only perturbed to the second order in ζ . Here, for $x_c = 0.5$, the χ_{sc} only changes by $\sim 11\%$ between two ensembles [131], which might look a bit small. However, considering that a polymer does not swell in the mixed poor solvents, an estimate of 11% is reasonable using Equation (14).

4. Design of Complex Copolymers in Mixed Solvents

The constant quest towards the design of polymer (or “smart” polymer) architectures for a range of advanced functional materials is at the heart of establishing a functional understating of their structure–property relationship [138–141]. In this context, the solution processing of these systems has a wide range of practical applications in biomedical encapsulation [38,39], artificial muscle tissues [19,139,142], “pick-up and place” systems [143], and biomedical glues [141]. These applications usually require a careful variation of the external stimuli. For this purpose, a variety of copolymer architectures are proposed here that can be used for a better conformational predictability and, thus, a better control on their functionalities. This includes sequences of smart polymers [16,18,36,84,144], copolymer sequences of smart and standard polymers [22,43], conventional copolymers [37], pluronics [37,39], and/or elastin-based peptides [15,77,78].

The temperature responsiveness is a commonly used external stimulus for tuning conformations in aqueous environments [16,18,22,37,39,40,145–148]. However, a lesser-investigated topic is a design principle using cosolvent effects [77,78,84,144,149]. This is particularly the case because a grand challenge here is to find a multicomponent copolymer sequence where different monomer units show contrasting conformational behavior in the same solvent–cosolvent mixtures. In this context, one possible combination may be the copolymers consisting of PNIPAM and poly(2-(methacryloyloxy)ethylphosphorylcholine) (PMPC) in aqueous alcohol mixtures [144]. This system is interesting because, while PNIPAM shows co-nonsolvency in the water-rich region [53,54], PMPC collapses in the alcohol-rich region [57]. This leads to an interesting conformational behavior of a single chain that results in p(NIPAM–co–MPC); see the simulation data in Figure 12a. The direct consequence of this behavior is the observation of reversible miscellization at a finite concentration of the p(NIPAM–co–MPC); the Cryo–TEM measurements in Figure 12b,c show the micelle formation.

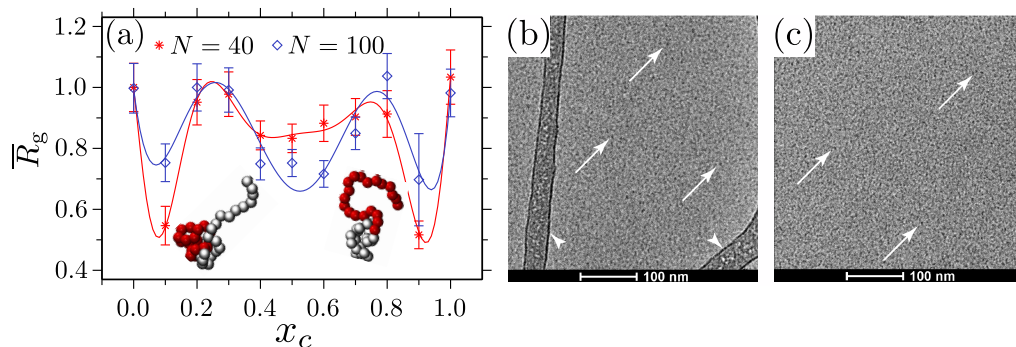


Figure 12. Part (a) shows the normalized radius of gyration $\bar{R}_g(x_c)/\bar{R}_g(x_c = 0)$ for a diblock copolymer as a function of cosolvent mole fraction x_c for two different chain lengths N_ℓ . Data are shown for the generic model for infinite polymer dilution, i.e., a single-chain conformation. The generic model mimics the conformations of a diblock consisting of poly(N-isopropylacrylamide) (PNIPAM) and a poly(2-(methacryloyloxy)ethylphosphorylcholine) (PMPC) blocks in aqueous alcohol mixtures. The simulation snapshots are shown for $x_c = 0.1$ (when the PNIPAM block collapses, shown as red beads) and for $x_c = 0.9$ (when the PMPC block collapses, shown as silver beads). Parts (b,c) show the Cryo–TEM images of p(NIPAM–co–MPC) for two ethanol volume fractions: (b) 0.04 and (c) 0.74, respectively. The core of the polymer micelles are highlighted by the white arrows. These figures have been reproduced with permission from the American Chemical Society [144].

Random sequences of the PNIPAM and PMPC show even more interesting conformations depending on the (co)solvent interaction contrast, the sequence lengths, and the monomer types; see the Supplementary Figure in Ref. [144]. Another possible system is a combination of monomers where one block shows co-nonsolvency, and the other shows cosolvency. One such example is a PMMA–PNIPAM diblock copolymer in aqueous alcohol mixtures [149]. In this case, the PNIPAM block collapses in the water-rich region (i.e.,

co-nonsolvency occurs) [53,54], and the PMMA block swells in the alcohol-rich region (i.e., cosolvency occurs) [126–128].

5. Heat Flow in Smart Polymers

In the preceding sections, we have presented an overview of the solution processable “smart” responsive polymers. Here, the applications of smart polymers are not only restricted to their dilute solutions; rather, they are also used for the thermal switching and also in designing lightweight high-performance organic solids. The main goal here is to provide a guiding path toward designing a set of biocompatible commodity polymeric materials with tunable thermal properties [150–154]. In this context, one of the central properties that often dictates the broad applicability of smart polymer or polymer-based materials is the ability to conduct the heat current, as quantified by the thermal transport coefficient κ [150,154]. For example, when a material is used under high-temperature conditions, such as the organic solar cells, the electronic packaging, and/or the heat sinking systems, a high κ is needed [151,152,155]. Low κ materials are required for their possible use in thermoelectrics [156]. Therefore, this poses a need to achieve a predictive tunability in κ .

Traditionally, most studies on thermal transport have attempted to unveil the structure–property relationship in nanomaterials [157–162]. Recent interest has been devoted to studying κ behavior in macromolecular systems [151–153,155,163–169] because of the inherent advantage of polymers in designing advanced functional materials. Therefore, in the following, we will highlight two related, yet distinct, topics that are relevant in the context of the heat flow in organic materials: (1) thermal switching controlled via coil-to-globule transition and (2) the heat flow in organic solids.

5.1. Thermal Switching in Smart Responsive Polymers

Heat management in advanced materials for a broad range of applications requires a very delicate control of their thermal switching. These applications span across thermoelectric energy conversion, energy storage, space technology, and sensing. Traditionally, the performance of thermal switches often suffers from slow transition rates [165,166,170]. Here, thermoresponsive smart polymers may serve as the suitable candidates. Particularly, a slight change in the external stimulus can significantly alter the structure, function, and stability of the smart polymers and, thus, may be used for fast switching in these systems.

In recent times, the studies of the κ in polymer solutions have gained attention [165,166,171]. In particular, the conformational transition of PNIPAM [165] and PNIPAM-based hydrogels [166] in water have been shown to play a key role in dictating the heat flow. For example, Figure 13 shows that the κ of aqueous PNIPAM solutions follows the same trend as their LCST coil-to-globule transition, with $T_\ell \simeq 305$ K (or 32 °C) [5,21]. On the contrary, however, an opposite trend (i.e., the κ increases above T_{cloud}) has been observed for concentrated polymer solutions [172]. These distinct results show that the polymer concentration plays a key role in dictating the κ behavior in polymer solutions.

Typically, κ increases with increasing T in disordered systems, which is because of increased localized vibrations [173,174]. This behavior has been weakly observed for pure water data; see the black dataset in Figure 13. The rather counterintuitive κ behavior, i.e., the κ decreases with increasing T , can possibly be explained by the loss of hydrogen bonds and the resultant breaking of the water caging around a polymer [165,166]. This further consolidates the fact that there is a direct correlation between the conformation and the κ value. Here, however, it should be noted that the change in κ with T in PNIPAM solutions may not be solely due to the conformations; rather, a delicate balance between the conformation, water tetrahedrality near a polymer, and hydrogen bonding leads to the data obtained in Figure 13, which, to the best of our knowledge, is a rather open discussion.

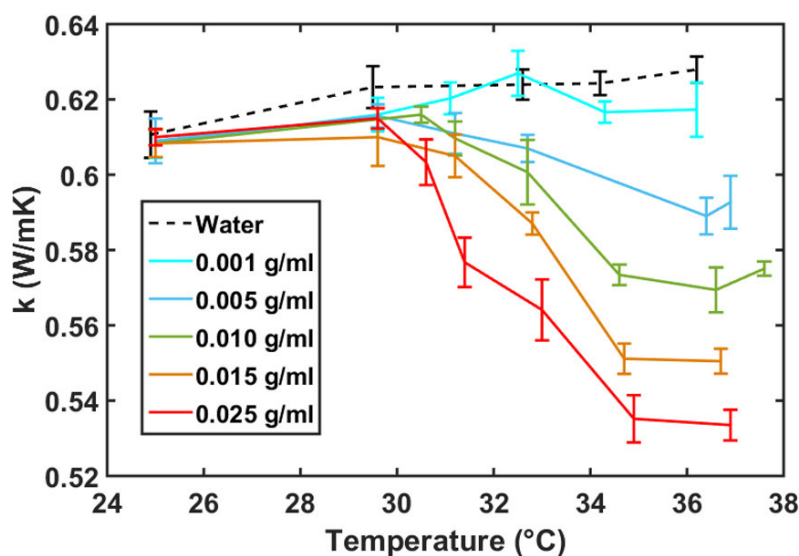


Figure 13. The thermal transport coefficient κ as a function of temperature T for the aqueous poly(*N*-isopropylacrylamide) (PNIPAM) solutions with changing PNIPAM concentrations. This figure has been reproduced with permission from the American Chemical Society [165].

5.2. Smart Polymers for Organic Solids

Organic solids (i.e., amorphous polymeric solids) are another class of materials where the H-bonded nature of the smart polymers can be used to tune their κ behavior. However, organic solids fall under the category of “low- κ ” materials [150–152,154]. For example, when polymer properties are dictated by weak vdW interactions $\kappa \leq 0.2$ W/Km, as is the case for PMMA, PS, and PAP [150,152,154,175]. In H-bonded systems (or “smart polymers”) where $\kappa \rightarrow 0.4$ W/Km, examples include PAA, PAM, PNIPAM, and PVA [151,152,176]. If we put the above κ values in perspective, a single-carbon nanotube (CNT) has $\kappa \geq 10^3$ W/Km [177], i.e., it is four orders of magnitude larger than the standard amorphous polymers. Attempts have been made to increase the κ of polymers by blending in high- κ materials, such as CNT or fullerene, within the amorphous polymers. This, however, requires the concentrations of the high- κ component to be larger than their percolation thresholds, and, thus, the original polymeric system loses all its flexibility. Therefore, a better alternative approach is to use the microscopic polymer interactions, conformation, morphology, and bond properties to achieve a tunable κ in polymers.

Polymers are a special case, because even when the macroscopic κ remains rather small, they have different microscopic pathways of energy transport [178,179]. More specifically, in an organic solid consisting of linear polymers, the energy can be transferred between two nonbonded monomers and between two covalently bonded monomers. A simple schematic of this energy transfer scheme is presented in Figure 14. Here, it is known that the rate of energy transfer between two bonded monomers is about 50–100 times faster than between two nonbonded monomers [163,179,180]. This is because the stiffness of a covalent contact is larger than 250 GPa [181], while the stiffness of a system that is purely dominated by nonbonded interactions may range between 2–5 GPa (vdW or H-bond) [152]. In this context, it is known that the stiffness is directly related to the κ [157,162] and, thus, is consistent with the faster energy transfer between the bonded monomers [179], as is evident from chain-oriented systems [163,180].

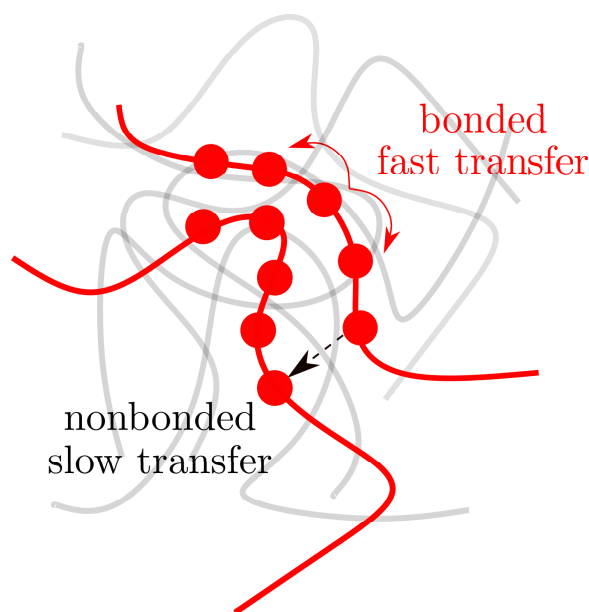


Figure 14. A schematic representation of the energy transfer pathways between two bonded (red arrows) and between two nonbonded (black arrow) monomers.

A simple model that connects the κ with the material stiffness is the minimum thermal conductivity model [157]:

$$\kappa^{\min} = \left(\frac{\pi}{432}\right)^{1/3} k_B^{1/3} c^{2/3} (v_l + 2v_t), \quad (15)$$

where c is the heat capacity. $v_l = \sqrt{C_{11}/\rho_m}$ and $v_t = \sqrt{C_{44}/\rho_m}$ are the longitudinal and transverse sound wave velocities, respectively. $C_{11} = K + 4C_{44}/3$, C_{44} is the shear modulus, K is the bulk modulus, and ρ_m is the mass density.

Equation (15) clearly indicates that, if the sound wave propagation (or stiffness) in a sample is tuned, it also helps with tuning the κ . Recently, tuning the κ values of organic solids has attracted great attention. This has been achieved via macromolecular engineering, which has included the following: (1) tuning the microscopic (nonbonded) interactions in linear polymers and polymer blends [150–154,182] and (2) by using covalent bonds [163,167–169,175,180,183,184].

5.2.1. Tuning κ via Nonbonded Interactions

A common protocol to tune the κ is by tuning the nonbonded interactions. Therefore, this poses a need to look beyond the standard single component polymeric systems, where the κ values remain rather restricted because of their predefined microscopic interactions. Here, a polymer blend with the desired combinations of polymers serves as a better candidate. In particular, a recent experimental study measured the $\kappa \rightarrow 1.5$ W/Km in an asymmetric blend consisting of short PAP and long PAA chains [151]; see the experimental data in Figure 15a. This κ enhancement was also shown to be directly related to an enhancement in the glass transition temperature T_g for a blend in comparison to the T_g of both of the individual components.

The main advantage of using such asymmetric systems is that they form a H-bonded crosslinked network, where the PAP molecules crosslink two PAA monomers from two different chains. A prerequisite of this protocol is that the PAP and PAA remain perfectly miscible over all monomer molar concentrations x_{PAP} . While the experimental data in Ref. [151] are extremely promising and show a significant improvement in the κ values, another independent set of experiments has argued that the PAP and PAA phases separate within a range of x_{PAP} , where a large enhancement in the κ was observed and where the $\kappa < 0.4$ W/Km over the full range of x_{PAP} [152]. The later experimental finding was also

confirmed by the simulation data where no enhancement in the κ was observed [153]; see the simulation data in Figure 15a.

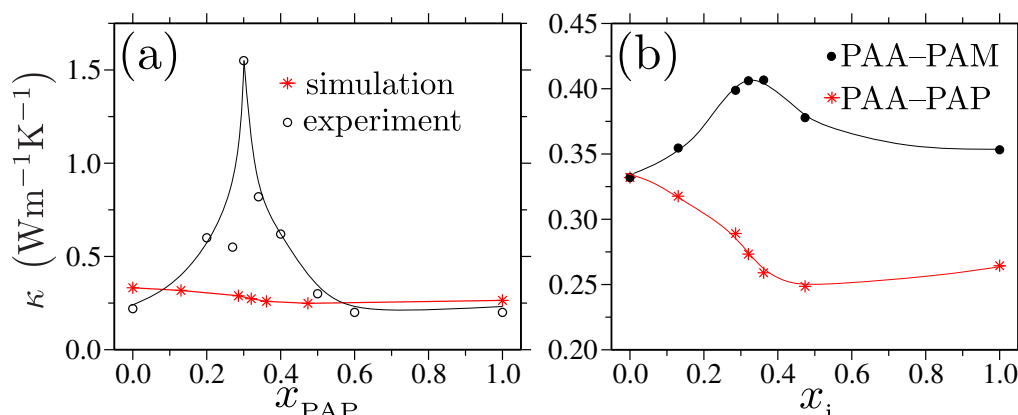


Figure 15. Part (a) shows the thermal transport coefficient κ for the blends of poly(acrylic acid) (PAA) and poly(N-acryloyl piperidine) (PAP) as a function of the PAP monomer mole fraction x_{PAP} [151]. Note that a separate set of experiments did not observe this large enhancement in κ in PAA–PAP blends [152]. Part (b) shows a comparative data for PAA–PAP and PAA and polyacrylamide (PAM) blends. These figures have been reproduced with permission from the American Chemical Society [153].

Going beyond these experiments, complementary simulation results also showed that the phase separation in PAP–PAA blends is triggered by the stacking of the aromatic side groups of different PAP molecules. Therefore, by introducing a modification in the monomer structure, i.e., by replacing the PAP with PAM, the miscibility of PAM–PAA blends can be greatly improved [153]. Even in this case, the maximum attainable κ remained below 0.4 W/Km ; see the black dataset in Figure 15b. These results further consolidate the fact that there might be an absolute maxima in the attainable κ of the amorphous organic solids consisting of neutral linear polymers or polymer blends, which is directly related to the limitations of the maximum attainable v_ℓ and v_t values [152]. This observation is independent of the specific chemical details and of the T_g , thus showing that neither of these system-specific quantities plays a key role in controlling the κ [176].

Typical systems where the κ may be improved beyond the maximum limit of 0.4 W/Km include, but are not limited to, polyelectrolytes, semicrystalline polymers, and/or polymers under high pressures. In the case of polyelectrolytes, it was shown that the change in the degree of ionization could increase the $\kappa \rightarrow 0.6 \text{ W/Km}$ for PAA [185], which was attributed to improved vdW forces due to electrostatic attractions. A similar argument may also hold for the case when a polymeric system is subjected to high pressures [186], where $\kappa \rightarrow 1.0 \text{ W/Km}$. Other examples include the systems consisting of complex monomer structures, where $\pi - \pi$ stacking leads to semicrystalline orders and, thus, to potentially increasing the κ [155,156]. Within the same spirit, polypeptides can also be used, where the fraction of the secondary structure (or the degree of crystallinity) leads to a significant increase in the κ [164].

5.2.2. Tuning κ via Bonded Interactions

Taking motivation from the observed significantly higher energy transfer rates between bonded monomers in comparison to nonbonded monomers, systems have been synthesized where the properties were dominated by bonded interactions. The systems where properties are dominated by the covalent bonds are chain-oriented systems (such as polymer fibers and molecular forests) [163,175,180] and crosslinked networks (such as epoxies and vitrimers) [167–169,183,184]. While the chain-oriented systems showed the $\kappa \rightarrow 100 \text{ W/Km}$ [163], the maximum attainable $\kappa \simeq 0.3 \text{ W/Km}$ was observed for the epoxies [167,184]. Even when the epoxies usually have a very high density of bonds, they

still have a rather small κ . This is particularly because the heat flow in epoxies is dictated by a delicate balance between bond types [167,183,184] and complex microstructures [167]. Epoxies with a certain degree of crystalline order can show a bit of a higher κ value. For example, semicrystalline epoxies have shown the $\kappa \rightarrow 0.5$ W/Km [168,169], and, for the liquid crystalline epoxies, they have shown the $\kappa \rightarrow 1.0$ W/km [187].

Note that, even though epoxies have been widely known for several decades as lightweight high-performance materials, they have found renewed attention within the last 2–3 years within the constant quest toward increasing the κ values of organic solids. Here, we only sketch a very short highlight of the heat flow in epoxies. Given that these are rather complex systems, a solid discussion is a topic of its own. This will be presented in a different note.

5.3. Classical Simulations and Comparing κ with the Experimental Data

Lastly, we would like to briefly comment on the calculated κ_{cla} within classical setups and their comparisons with the experimental data κ_{exp} . In this context, the results indicate that the $\kappa_{\text{cla}} > \kappa_{\text{exp}}$ [176,188,189]. This is the case even when the simulations have been conducted using the most accurate (available) empirical potentials, as well as when the κ_{cla} values have been calculated very carefully. Here, it is important to highlight that this discrepancy between the κ_{cla} and κ_{exp} is not a technical issue; rather, it is a more fundamental issue. For example, as highlighted in Equation (15), the heat flow is directly related to the c and v . If any of the c and v are calculated inaccurately, this automatically leads to the wrong κ_{cla} estimates. In this context, one of the major contributions to the error in κ_{cla} calculations is the inaccurate estimates of the c within classical simulation setups [190–192].

Within the classical description, the Dulong–Petit limit yields $c = 3Nk_B$, i.e., all modes contribute equally to the total c . In reality, however, many modes in polymers are quantum-mechanically frozen at the room temperature of $T_{\text{room}} = 300$ K. For example, the C–H vibrational frequency (a common building block of polymers) is $\nu \simeq 90$ THz, while the $\nu_{\text{room}} \simeq 6.2$ THz at T_{room} [190]; see the vibrational density of the states $g(\nu)$ for an alkane system in Figure 16a. Similarly, there are other modes, such as the C–C bond and the H–C–H angular vibrations, that have ν values that are significantly larger than a $\nu_{\text{room}} \simeq 6.2$ THz. Even when these modes are excited at T_{room} , their contributions are automatically incorporated into the c and, thus, affect the κ_{cla} estimates. Therefore, unless the κ_{cla} is reweighted to account for the quantum corrections to c , reasonable comparisons may be difficult to achieve within the classical setups.

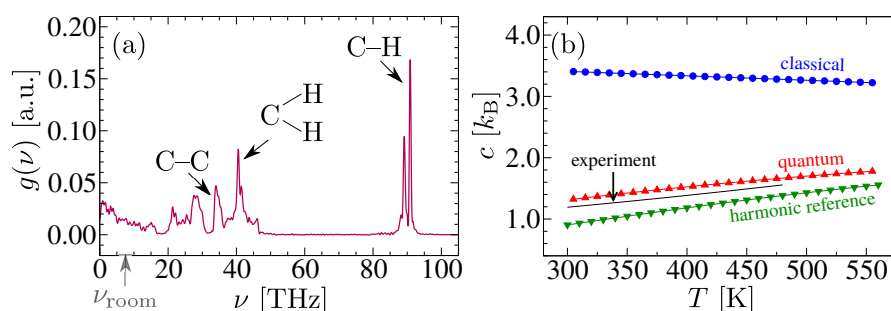


Figure 16. Part (a) shows the vibrational density of states $g(\nu)$ for hexadecane calculated using Equation (17). A few vibrational modes are highlighted as the legends. Part (b) shows a comparison between the specific heat c calculated in simulations by different methods and measured in experiments. These figures have been reproduced with permission from the American Physical Society [190].

An earlier experimental study proposed a simplified correction to c in Equation (15). This approach proposed a corrected estimate using $c_{\text{cor}} = 3N_{\text{cor}}k_B$, where $N_{\text{cor}} = 2(N - N_H)/3$ accounts for the contributions of the stiff modes [186], and N_H is the number of

hydrogen atoms in a system. While this approximation gives reasonably accurate estimates [157,186], it will also be important to have a method that uses a solid theoretical basis.

One method to calculate the c_{cor} is the harmonic reference proposed in Ref. [193]. Here, if the frequency of a (stiff) harmonic mode is known, this mode contributes $k_B(h\nu/2k_B T)^2/\sinh^2(h\nu/2k_B T)$ to the c_{cor} . Then, the total equates to the following:

$$c_{\text{cor}}(T) = k_B \int_0^\infty \frac{(h\nu/2k_B T)^2}{\sinh^2(h\nu/2k_B T)} g(\nu) d\nu. \quad (16)$$

Within the harmonic approximation, the $g(\nu)$ can be calculated using the following formula:

$$g(\nu) = \frac{1}{G} \int_0^\infty dt \cos(2\pi\nu\Delta t) \frac{C(\Delta t)}{C(0)}, \quad (17)$$

where $C(\Delta t) = \sum_n m_n \langle \mathbf{v}_n(t) \cdot \mathbf{v}_n(t + \Delta t) \rangle$ is the mass-weighted velocity autocorrelation function, and G ensures that $\int_0^\infty g(\nu) d\nu = 1$. Note that, in a harmonic system, the $C(\Delta t)$ results from the superposition of individual normal modes and their Fourier transforms make it possible to determine what percentage of modes have what resonance frequencies. The result using Equation (16) showed a good agreement with the experimental data; see the green data set (harmonic reference) in Figure 16b.

A more recent method, particularly tuned for the liquid polymers, used Equation (16) to estimate the difference between the classical and the quantum systems by using the following equation:

$$\Delta c_{\text{rel}}(T) = \int_0^\infty \left\{ 1 - \frac{(h\nu/2k_B T)^2}{\sinh^2(h\nu/2k_B T)} \right\} g(\nu) d\nu, \quad (18)$$

and the method then used $c_{\text{cor}}(T) = c_{\text{cla}}(T) - \Delta c_{\text{rel}}(T)$ [190]. Here, $c_{\text{cla}} = [H(T - \Delta T) - H(T + \Delta T)]/2\Delta T$, and $H(T)$ is the enthalpy. The main advantage of the later approach is that the stiff harmonic modes are corrected, while the contributions from the anharmonic modes remain unaltered, which is absolutely important for polymeric systems. This approach also yielded a good agreement with the experimental data; see the red dataset (quantum) in Figure 16b.

The method proposed in Ref. [190] also highlighted different strategies to estimate the c_{cor} to account for the missing degrees of freedom (DOF) within the united-atom and/or coarse-grained models [190]. A direct implication is that a certain percentage error in the κ calculations using the united-atom models comes from the missing DOFs [173].

6. Concluding Remarks

The field of polymer research has grown quite significantly over the last few decades, where many new exciting topics and systems are being constantly investigated using experimental, computational, and analytical tools. Smart responsive polymers are one such exciting class that has gained tremendous attention over the last decade. These systems are not only important because of their biocompatible and thermoresponsive nature, but also because they often show counterintuitive solvation behaviors in mixtures of solvents. Therefore, it is often challenging to develop the microscopic structure–function relationship in these systems, while they have tremendous technological relevance that spans across biomedical applications [19,38,39,139,142], adhesive polymer-coated surfaces [141,143,194], and biocompatible commodity organic solids [150–154,156].

In this review, we have presented a brief overview of the present state of smart polymer research. We began with discussing the polymer conformations in single and multicomponent mixtures. In particular, we discussed two opposite phenomena, namely, co-nonsolvency and cosolvency. While co-nonsolvency is associated with the collapse of a polymer in the mixtures of two miscible good solvents, cosolvency is a term given to a phenomenon when a polymer swells in poor solvent mixtures. The present state of

understanding proposed by the simulation and analytical tools was discussed, together with the complementary experiments. A generic picture has been presented that highlights that these two phenomena are not restricted to a few specific systems; rather, a broad range of polymers shows such solvation behavior in their respective mixtures of solvents. One system that requires special mention is the PMMA system, which shows both co-solvency [79] and cosolvency [126–128] behaviors. We have also highlighted how smart polymeric materials may be used as the guiding path toward designing advanced materials with tunable and predictive responsiveness.

This review also highlighted the possible applications of smart polymers for biocompatible organic solids, which is a topic that has gained a lot of attention over the last decade. Within this topic, one central property of interest is the thermal conductivity coefficient κ , which is of great importance because of the possible use of organic solids for various applications. For example, amorphous organic solids consisting of linear polymers or linear polymer blends have very low κ values that may provide a good material choice when they are used as thermoelectrics. However, this low- κ behavior also poses great problems when an organic solid is used under high-temperature conditions. Therefore, a large number of works has devoted significant efforts to achieving a large κ for organic solids via macromolecular engineering. This has ranged from tuning the nonbonded interactions in polymer blends to employing highly crosslinked polymer networks where bonded interactions are dominant.

Lastly, we want to conclude by commenting that, even though we briefly covered two distinct applications of smart polymers, it was still impossible to cover all aspects of this exciting research topic. More specifically, we have predominantly based our discussions on neutral polymers in mixed solvents and in their amorphous solid states. However, there are several other topics that are important within the smart polymer research, especially when dealing with the polymers in ionic solutions, electrolytes, organic electronics, and semicrystalline and liquid crystalline epoxy networks. These are only a few (out of many) exciting systems that we could not cover in this review, but we hope that the discussion presented here might provide some basics regarding the present state of smart polymer research that may stimulate further discussions on this topic.

Author Contributions: D.M. and K.K. designed the content of this review. D.M. structured the contents and wrote this draft with comments from K.K. All authors have read and agreed to the published version of the manuscript.

Funding: This research received no external funding.

Acknowledgments: The contents presented in this review have greatly benefited from very fruitful collaborations with more than seventy colleagues over the last decade, to whom we take this opportunity to gratefully acknowledge. In particular, we thank Carlos Marques for a very fruitful continual collaboration in theory polymer solutions. We further thank Tiago Espinosa de Oliveira, Robinson Cortes-Huerto, Manfred Wagner, Yani Zhao, Jeffrey Koberstein, Regine von Klitzing, and Tanja Weil for various simulation and experimental collaborations in smart polymer solvation. D.M. thanks Marcus Müller and Martin Müser for two very fruitful collaborations in the calculations of monomer-level energy transfer rates and the accurate specific heat calculation of polymers that led to the foundations of some of the discussions presented in this review. James Wu, Aashish Bhardwaj, Celine Ruscher, A. Srikantha Phani, Manoj Maurya, Alireza Nojeh, Jörg Rottler, Daniel Bruns, and Manjesh Singh are acknowledged for their various collaborations at the different stages of the thermal transport projects. D.M. further thanks the Canada First Research Excellence Fund (CFREF) and the Quantum Materials and Future Technologies Program. We thank Robinson Cortes-Huerto for a critical reading of this draft, as well as Robinson Cortes-Huerto and Yani Zhao for providing a few figures for our collaborative publications [78,110].

Conflicts of Interest: The authors declare no conflict of interest.

References

1. Staudinger, H. Uber Polymerisation. *Eur. J. Inorg. Chem.* **1920**, *53*, 1073–1085. [[CrossRef](#)]
2. Köger, M. Simple models for complex nonequilibrium fluids. *Phys. Rep.* **2004**, *390*, 453–551. [[CrossRef](#)]
3. Cohen-Stuart, M.A.; Huck, W.T.S.; Genzer, J.; Müller, M.; Ober, C.; Stamm, M.; Sukhorukov, G.B.; Szleifer, I.; Tsukruk, V.V.; Urban, M.; et al. Emerging applications of stimuli-responsive polymer materials. *Nat. Mater.* **2010**, *9*, 101–113. [[CrossRef](#)]
4. Zhang, Q.; Hoogenboom, R. Polymers with upper critical solution temperature behavior in alcohol/water solvent mixtures. *Prog. Polym. Sci.* **2015**, *48*, 122–142. [[CrossRef](#)]
5. Halperin, A.; Kröger, M.; Winnik, F.M. Poly(N-isopropylacrylamide) Phase Diagrams: Fifty Years of Research. *Angew. Chem. Int. Ed.* **2015**, *54*, 15342–15367. [[CrossRef](#)]
6. Gao, H.; Bettscheider, S.; Kraus, T.; Müser, M.H. Entropy Can Bundle Nanowires in Good Solvents. *Nano Lett.* **2019**, *19*, 6993–6999. [[CrossRef](#)] [[PubMed](#)]
7. Müller, M. Process-directed self-assembly of copolymers: Results of and challenges for simulation studies. *Prog. Polym. Sci.* **2020**, *101*, 101198. [[CrossRef](#)]
8. Mukherji, D.; Marques, C.M.; Kremer, K. Smart responsive polymers: Fundamentals and design principles. *Annu. Rev. Condens. Matter Phys.* **2020**, *11*, 271–299. [[CrossRef](#)]
9. Chen, C.; Ng, D.Y.W.; Weil, T. Polymer bioconjugates: Modern design concepts toward precision hybrid materials. *Prog. Polym. Sci.* **2020**, *105*, 101241. [[CrossRef](#)]
10. Forero-Martinez, N.C.; Lin, K.H.; Kremer, K.; Andrienko, D. Virtual Screening for Organic Solar Cells and Light Emitting Diodes. *Adv. Sci.* **2022**, *9*, 2200825. [[CrossRef](#)]
11. Mendrek, B.; Oleszko-Torbus, N.; Teper, P.; Kowalczyk, A. Towards next generation polymer surfaces: Nano- and microlayers of star macromolecules and their design for applications in biology and medicine. *Prog. Polym. Sci.* **2023**, *139*, 101657. [[CrossRef](#)]
12. Doi, M.; Edwards, S.F. *The Theory of Polymer Dynamics*; Oxford Science Publications: Oxford, UK, 1986.
13. de Gennes, P.G. *Scaling Concepts in Polymer Physics*; Cornell University Press: Ithaca, NY, USA, 1979.
14. Cloizeaux, J.D.; Jannink, G. *Polymers in Solution: Their Modelling and Structure*; Clarendon Press: Oxford, UK, 1990.
15. Meyer, D.E.; Chilkoti, A. Purification of recombinant proteins by fusion with thermally-responsive polypeptides. *Nat. Biotechnol.* **1999**, *17*, 1112–1115. [[CrossRef](#)] [[PubMed](#)]
16. Li, C.; Buurma, N.J.; Haq, I.; Turner, C.; Armes, S.P.; Castelletto, V.; Hamley, I.W.; Lewis, A.L. Synthesis and Characterization of Biocompatible, Thermoresponsive ABC and ABA Triblock Copolymer Gelators. *Langmuir* **2005**, *21*, 11026–11033. [[CrossRef](#)] [[PubMed](#)]
17. Zhang, Y.; Furyk, S.; Bergbreiter, D.E.; Cremer, P.S. Specific Ion Effects on the Water Solubility of Macromolecules: PNIPAM and the Hofmeister Series. *J. Am. Chem. Soc.* **2005**, *127*, 14505–14510. [[CrossRef](#)] [[PubMed](#)]
18. Lutz, J.F.; Akdemir, Ö.; Hoth, A. Point by Point Comparison of Two Thermosensitive Polymers Exhibiting a Similar LCST: Is the Age of Poly(NIPAM) Over? *J. Am. Chem. Soc.* **2006**, *128*, 13046–13047. [[CrossRef](#)] [[PubMed](#)]
19. Cui, S.; Pang, X.; Zhang, S.; Yu, Y.; Ma, H.; Zhang, X. Unexpected Temperature-Dependent Single Chain Mechanics of Poly(N-isopropyl-acrylamide) in Water. *Langmuir* **2012**, *28*, 5151–5157. [[CrossRef](#)]
20. Desiraju, G.R. Hydrogen Bridges in Crystal Engineering: Interactions without Borders. *Accounts Chem. Res.* **2002**, *35*, 565–573. [[CrossRef](#)]
21. Wu, C.; Wang, X. Globule-to-Coil Transition of a Single Homopolymer Chain in Solution. *Phys. Rev. Lett.* **1998**, *80*, 4092–4094. [[CrossRef](#)]
22. Samanta, S.; Bogdanowicz, D.R.; Lu, H.H.; Koberstein, J.T. Polyacetals: Water-Soluble, pH-Degradable Polymers with Extraordinary Temperature Response. *Macromolecules* **2016**, *49*, 1858–1864. [[CrossRef](#)]
23. de Oliveira, T.E.; Mukherji, D.; Kremer, K.; Netz, P.A. Effects of stereochemistry and copolymerization on the LCST of PNIPAm. *J. Chem. Phys.* **2017**, *146*, 034904. [[CrossRef](#)]
24. Chen, S.; Wang, K.; Zhang, W. A new thermoresponsive polymer of poly(N-acryloylsarcosine methyl ester) with a tunable LCST. *Polym. Chem.* **2017**, *8*, 3090–3101. [[CrossRef](#)]
25. Kratz, K.; Hellweg, T.; Eimer, W. Structural changes in PNIPAM microgel particles as seen by SANS, DLS, and EM techniques. *Polymer* **2001**, *42*, 6631–6639. [[CrossRef](#)]
26. Scherzinger, C.; Holderer, O.; Richter, D.; Richtering, W. Polymer dynamics in responsive microgels: Influence of cononsolvency and microgel architecture. *Phys. Chem. Chem. Phys.* **2012**, *14*, 2762–2768. [[CrossRef](#)]
27. Backes, S.; Krause, P.; Tabaka, W.; Witt, M.U.; Mukherji, D.; Kremer, K.; von Klitzing, R. Poly(N-isopropylacrylamide) Microgels under Alcoholic Intoxication: When a LCST Polymer Shows Swelling with Increasing Temperature. *ACS Macro Lett.* **2017**, *6*, 1042–1046. [[CrossRef](#)]
28. Kawasaki, H.; Nakamura, T.; Miyamoto, K.; Tokita, M.; Komai, T. Multiple volume phase transition of nonionic thermosensitive gel. *J. Chem. Phys.* **1995**, *103*, 6241–6247. [[CrossRef](#)]
29. de Oliveira, T.E.; Marques, C.M.; Netz, P.A. Molecular dynamics study of the LCST transition in aqueous poly(N-n-propylacrylamide). *Phys. Chem. Chem. Phys.* **2018**, *20*, 10100–10107. [[CrossRef](#)]
30. Landau, L.D.; Lifshitz, E.M. *Statistical Physics*, 3rd ed.; Elsevier Butterworth-Heinemann: Oxford, UK, 2003.
31. Jeppesen, C.; Kremer, K. Single-chain collapse as a first-order transition: Model for PEO in water. *Europhys. Lett.* **1996**, *34*, 563. [[CrossRef](#)]

32. Oh, S.Y.; Yang, H.E.; Bae, Y.C. Molecular simulations and thermodynamic modeling for closed-loop phase miscibility of aqueous PEO solutions. *Macromol. Res.* **2013**, *21*, 921–930. [[CrossRef](#)]
33. Hocine, S.; Li, M.H. Thermoresponsive self-assembled polymer colloids in water. *Soft Matter* **2013**, *9*, 5839–5861. [[CrossRef](#)]
34. Badi, N. Non-linear PEG-based thermoresponsive polymer systems. *Prog. Polym. Sci.* **2017**, *66*, 54–79. [[CrossRef](#)]
35. Gernandt, J.; Frenning, G.; Richtering, W.; Hansson, P. A model describing the internal structure of core/shell hydrogels. *Soft Matter* **2011**, *7*, 10327–10338. [[CrossRef](#)]
36. Zhou, Y.; Jiang, K.; Song, Q.; Liu, S. Thermo-Induced Formation of Unimolecular and Multimolecular Micelles from Novel Double Hydrophilic Multiblock Copolymers of N,N-Dimethylacrylamide and N-Isopropylacrylamide. *Langmuir* **2007**, *23*, 13076–13084. [[CrossRef](#)]
37. Kelley, E.G.; Smart, T.P.; Jackson, A.J.; Sullivan, M.O.; Epps, T.H. Structural changes in block copolymer micelles induced by cosolvent mixtures. *Soft Matter* **2011**, *7*, 7094–7102. [[CrossRef](#)] [[PubMed](#)]
38. Adams, M.L.; Lavasanifar, A.; Kwon, G.S. Amphiphilic block copolymers for drug delivery. *J. Pharm. Sci.* **2003**, *92*, 1343–1355. [[CrossRef](#)]
39. Batrakova, E.V.; Kabanov, A.V. Pluronic block copolymers: Evolution of drug delivery concept from inert nanocarriers to biological response modifiers. *J. Control. Release* **2008**, *130*, 98–106. [[CrossRef](#)] [[PubMed](#)]
40. Papadakis, C.M.; Müller-Buschbaum, P.; Laschewsky, A. Switch It Inside-Out: “Schizophrenic” Behavior of All Thermoresponsive UCST–LCST Diblock Copolymers. *Langmuir* **2019**, *35*, 9660–9676. [[CrossRef](#)]
41. Hoffman, A.S.; Stayton, P.S.; Bulmus, V.; Chen, G.; Chen, J.; Cheung, C.; Chilkoti, A.; Ding, Z.; Dong, L.; Fong, R.; et al. Really smart bioconjugates of smart polymers and receptor proteins. *J. Biomed. Mater. Res.* **2000**, *52*, 577–586. [[CrossRef](#)]
42. Shen, Z.; Terao, K.; Maki, Y.; Dobashi, T.; Ma, G.; Yamamoto, T. Synthesis and phase behavior of aqueous poly(N-isopropylacrylamide-co-acrylamide), poly(N-isopropylacrylamide-co-N,N-dimethylacrylamide) and poly(N-isopropylacrylamide-co-2-hydroxyethyl methacrylate). *Colloid Polym. Sci.* **2006**, *284*, 1001. [[CrossRef](#)]
43. De Silva, C.C.; Leophairatana, P.; Ohkuma, T.; Koberstein, J.T.; Kremer, K.; Mukherji, D. Sequence transferable coarse-grained model of amphiphilic copolymers. *J. Chem. Phys.* **2017**, *147*, 064904. [[CrossRef](#)]
44. Tschöp, W.; Kremer, K.; Batoulis, J.; Bürger, T.; Hahn, O. Simulation of polymer melts. I. Coarse-graining procedure for polycarbonates. *Acta Polym.* **1998**, *49*, 61–74. [[CrossRef](#)]
45. Tschöp, W.; Kremer, K.; Hahn, O.; Batoulis, J.; Bürger, T. Simulation of polymer melts. II. From coarse-grained models back to atomistic description. *Acta Polym.* **1998**, *49*, 75–79. [[CrossRef](#)]
46. de Oliveira, T.E.; Netz, P.A.; Kremer, K.; Junghans, C.; Mukherji, D. C-IBI: Targeting cumulative coordination within an iterative protocol to derive coarse-grained models of (multi-component) complex fluids. *J. Chem. Phys.* **2016**, *144*, 174106. [[CrossRef](#)] [[PubMed](#)]
47. Meyer, D.E.; Chilkoti, A. Genetically Encoded Synthesis of Protein-Based Polymers with Precisely Specified Molecular Weight and Sequence by Recursive Directional Ligation: Examples from the Elastin-like Polypeptide System. *Biomacromolecules* **2002**, *3*, 357–367. [[CrossRef](#)]
48. McPherson, D.T.; Xu, J.; Urry, D.W. Product Purification by Reversible Phase Transition Following Escherichia coli Expression of Genes Encoding up to 251 Repeats of the Elastomeric Pentapeptide GVGVP. *Protein Expr. Purif.* **1996**, *7*, 51–57. [[CrossRef](#)] [[PubMed](#)]
49. Zhao, B.; Li, N.K.; Yingling, Y.G.; Hall, C.K. LCST Behavior is Manifested in a Single Molecule: Elastin-like polypeptide (VPGVG)_n. *Biomacromolecules* **2016**, *17*, 111–118. [[CrossRef](#)]
50. Prashanna, A.; Taylor, P.A.; Qin, J.; Kiick, K.L.; Jayaraman, A. Effect of Peptide Sequence on the LCST-like Transition of Elastin-like Peptides and Elastin-like Peptide–Collagen-like Peptide Conjugates: Simulations and Experiments. *Biomacromolecules* **2019**, *20*, 1178–1189. [[CrossRef](#)]
51. Dugave, C.; Demange, L. Cis-Trans Isomerization of Organic Molecules and Biomolecules: Implications and Applications. *Chem. Rev.* **2003**, *103*, 2475–2532. [[CrossRef](#)]
52. Zhao, Y.; Kremer, K. Proline Isomerization Regulates the Phase Behavior of Elastin-like Polypeptides in Water. *J. Phys. Chem. B* **2021**, *125*, 9751–9756. [[CrossRef](#)]
53. Schild, H.G.; Muthukumar, M.; Tirrell, D.A. Cononsolvency in mixed aqueous solutions of poly(N-isopropylacrylamide). *Macromolecules* **1991**, *24*, 948–952. [[CrossRef](#)]
54. Winnik, F.M.; Ringsdorf, H.; Venzmer, J. Methanol-water as a co-nonsolvent system for poly(N-isopropylacrylamide). *Macromolecules* **1990**, *23*, 2415–2416. [[CrossRef](#)]
55. Zhang, G.; Wu, C. Reentrant Coil-to-Globule-to-Coil Transition of a Single Linear Homopolymer Chain in a Water-Methanol Mixture. *Phys. Rev. Lett.* **2001**, *86*, 822–825. [[CrossRef](#)]
56. Hiroki, A.; Maekawa, Y.; Yoshida, M.; Kubota, K.; Katakai, R. Volume phase transitions of poly(acryloyl-L-proline methyl ester) gels in response to water–alcohol composition. *Polymer* **2001**, *42*, 1863–1867. [[CrossRef](#)]
57. Kiritoshi, Y.; Ishihara, K. Preparation of cross-linked biocompatible poly(2-methacryloyloxyethyl phosphorylcholine) gel and its strange swelling behavior in water/ethanol mixture. *J. Biomater. Sci. Polym. Ed.* **2002**, *13*, 213–224. [[CrossRef](#)] [[PubMed](#)]
58. Tanaka, F.; Koga, T.; Winnik, F.M.C.M. Temperature-Responsive Polymers in Mixed Solvents: Competitive Hydrogen Bonds Cause Cononsolvency. *Phys. Rev. Lett.* **2008**, *101*, 028302. [[CrossRef](#)] [[PubMed](#)]

59. Sagle, L.B.; Zhang, Y.; Litosh, V.A.; Chen, X.; Cho, Y.; Cremer, P.S. Investigating the Hydrogen-Bonding Model of Urea Denaturation. *J. Am. Chem. Soc.* **2009**, *131*, 9304–9310. [[CrossRef](#)]
60. Kojima, H.; Tanaka, F.; Scherzinger, C.; Richtering, W. Temperature dependent phase behavior of PNIPAM microgels in mixed water/methanol solvents. *J. Polym. Sci. Part B Polym. Phys.* **2013**, *51*, 1100–1111. [[CrossRef](#)]
61. Walter, J.; Sehr, J.; Vrabec, J.; Hasse, H. Molecular Dynamics and Experimental Study of Conformation Change of Poly(N-isopropylacrylamide) Hydrogels in Mixtures of Water and Methanol. *J. Phys. Chem. B* **2012**, *116*, 5251–5259. [[CrossRef](#)]
62. Heyda, J.; Muzdalo, A.; Dzubiella, J. Rationalizing Polymer Swelling and Collapse under Attractive Cosolvent Conditions. *Macromolecules* **2013**, *46*, 1231–1238. [[CrossRef](#)]
63. Mukherji, D.; Kremer, K. Coil–Globule–Coil Transition of PNIPAM in Aqueous Methanol: Coupling All-Atom Simulations to Semi-Grand Canonical Coarse-Grained Reservoir. *Macromolecules* **2013**, *46*, 9158–9163. [[CrossRef](#)]
64. Bischofberger, I.; Calzolari, D.C.E.; Trappe, V. Co-nonsolvency of PNIPAM at the transition between solvation mechanisms. *Soft Matter* **2014**, *10*, 8288–8295. [[CrossRef](#)]
65. Dudowicz, J.; Freed, K.F.; Douglas, J.F. Communication: Cosolvency and consolvency explained in terms of a Flory-Huggins type theory. *J. Chem. Phys.* **2015**, *143*, 131101. [[CrossRef](#)]
66. Kyriakos, K.; Philipp, M.; Lin, C.H.; Dyakonova, M.; Vishnevetskaya, N.; Grillo, I.; Zaccone, A.; Miasnikova, A.; Laschewsky, A.; Müller-Buschbaum, P.; et al. Quantifying the Interactions in the Aggregation of Thermoresponsive Polymers: The Effect of Consolvency. *Rapid Commun.* **2016**, *37*, 420–425. [[CrossRef](#)]
67. Micciulla, S.; Michalowsky, J.; Schroer, M.A.; Holm, C.; von Klitzing, R.; Smiatek, J. Concentration dependent effects of urea binding to poly(N-isopropylacrylamide) brushes: A combined experimental and numerical study. *Phys. Chem. Chem. Phys.* **2016**, *18*, 5324–5335. [[CrossRef](#)] [[PubMed](#)]
68. Zhu, P.w.; Chen, L. Effects of cosolvent partitioning on conformational transitions and chain flexibility of thermoresponsive microgels. *Phys. Rev. E* **2019**, *99*, 022501. [[CrossRef](#)] [[PubMed](#)]
69. Zhu, P.W. Effects of cosolvent partitioning on conformational transitions and tethered chain flexibility in spherical polymer brushes. *Soft Matter* **2021**, *17*, 6817–6832. [[CrossRef](#)]
70. Pérez-Ramírez, H.A.; Haro-Pérez, C.; Vázquez-Contreras, E.; Klapp, J.; Bautista-Carbajal, G.; Odriozola, G. P-NIPAM in water–acetone mixtures: Experiments and simulations. *Phys. Chem. Chem. Phys.* **2019**, *21*, 5106–5116. [[CrossRef](#)] [[PubMed](#)]
71. Sakota, K.; Tabata, D.; Sekiya, H. Macromolecular Crowding Modifies the Impact of Specific Hofmeister Ions on the Coil–Globule Transition of PNIPAM. *J. Phys. Chem. B* **2015**, *119*, 10334–10340. [[CrossRef](#)]
72. Okur, H.I.; Hladílková, J.; Rembert, K.B.; Cho, Y.; Heyda, J.; Dzubiella, J.; Cremer, P.S.; Jungwirth, P. Beyond the Hofmeister Series: Ion-Specific Effects on Proteins and Their Biological Functions. *J. Phys. Chem. B* **2017**, *121*, 1997–2014. [[CrossRef](#)]
73. Shultz, A.R.; Flory, P.J. Polymer chain dimensions in mixed-solvent media. *J. Polym. Sci.* **1955**, *15*, 231–242. [[CrossRef](#)]
74. Read, B.E. A light-scattering study of preferential adsorption in the system benzene + cyclohexane + polystyrene. *Trans. Faraday Soc.* **1960**, *56*, 382–390. [[CrossRef](#)]
75. Wolf, B.A.; Willms, M.M. Measured and calculated solubility of polymers in mixed solvents: Co-nonsolvency. *Die Makromol. Chem.* **1978**, *179*, 2265–2277. [[CrossRef](#)]
76. Mukherji, D.; Wagner, M.; Watson, M.D.; Winzen, S.; de Oliveira, T.E.; Marques, C.M.; Kremer, K. *Soft Matter* **2016**, *12*, 7995–8003. [[CrossRef](#)]
77. Mills, C.E.; Ding, E.; Olsen, B.D. Consolvency of Elastin-like Polypeptides in Water/Alcohol Solutions. *Biomacromolecules* **2019**, *20*, 2167–2173. [[CrossRef](#)] [[PubMed](#)]
78. Zhao, Y.; Singh, M.K.; Kremer, K.; Cortes-Huerto, R.; Mukherji, D. Why Do Elastin-like Polypeptides Possibly Have Different Solvation Behaviors in Water-Ethanol and Water-Urea Mixtures? *Macromolecules* **2020**, *53*, 2101–2110. [[CrossRef](#)]
79. Fernandez-Pierola, I.; Horta, A. Co-nonsolvency of PMMA. *Polym. Bull.* **1980**, *3*, 273–278. [[CrossRef](#)]
80. Lund, R.; Willner, L.; Stellbrink, J.; Radulescu, A.; Richter, D. Role of Interfacial Tension for the Structure of PEP-PEO Polymeric Micelles. A Combined SANS and Pendant Drop Tensiometry Investigation. *Macromolecules* **2004**, *37*, 9984–9993. [[CrossRef](#)]
81. Ohkura, M.; Kanaya, T.; Keisuke, K. Gels of poly(vinyl alcohol) from dimethyl sulphoxide/water solutions. *Polymer* **1992**, *33*, 3686–3690. [[CrossRef](#)]
82. Jia, D.; Zuo, T.; Rogers, S.; Cheng, H.; Hammouda, B.; Han, C.C. Re-entrance of Poly(N,N-diethylacrylamide) in D₂O/d-Ethanol Mixture at 27 °C. *Macromolecules* **2016**, *49*, 5152–5159. [[CrossRef](#)]
83. Higaki, Y.; Kuraoka, N.; Masuda, T.; Nakamura, M.; Hifumi, E. Consolvency of poly(carboxybetaine methacrylate) in water–ethanol mixed solvents. *Polym. J.* **2023**, *55*, 869–876. [[CrossRef](#)]
84. Scherzinger, C.; Lindner, P.; Keerl, M.; Richtering, W. Consolvency of Poly(N,N-diethylacrylamide) (PDEAAM) and Poly(N-isopropylacrylamide) (PNIPAM) Based Microgels in Water/Methanol Mixtures: Copolymer vs Core-Shell Microgel. *Macromolecules* **2010**, *43*, 6829–6833. [[CrossRef](#)]
85. Tanaka, F.; Koga, T.; Kojima, H.; Xue, N.; Winnik, F.M. Preferential Adsorption and Co-nonsolvency of Thermoresponsive Polymers in Mixed Solvents of Water/Methanol. *Macromolecules* **2011**, *44*, 2978–2989. [[CrossRef](#)]
86. Mukherji, D.; Marques, C.M.; Kremer, K. Collapse in two good solvents, swelling in two poor solvents: Defying the laws of polymer solubility? *J. Phys. Condens. Matter* **2017**, *30*, 024002. [[CrossRef](#)] [[PubMed](#)]

87. Yong, H.; Merlitz, H.; Fery, A.; Sommer, J.U. Polymer Brushes and Gels in Competing Solvents: The Role of Different Interactions and Quantitative Predictions for Poly(N-isopropylacrylamide) in Alcohol–Water Mixtures. *Macromolecules* **2020**, *53*, 2323–2335. [[CrossRef](#)]
88. Mukherji, D.; Marques, C.M.; Kremer, K. Polymer collapse in miscible good solvents is a generic phenomenon driven by preferential adsorption. *Nat. Commun.* **2014**, *5*, 4882. [[CrossRef](#)] [[PubMed](#)]
89. Mukherji, D.; Marques, C.M.; Stuehn, T.; Kremer, K. Co-non-solvency: Mean-field polymer theory does not describe polymer collapse transition in a mixture of two competing good solvents. *J. Chem. Phys.* **2015**, *142*, 114903. [[CrossRef](#)]
90. Jia, D.; Muthukumar, M.; Cheng, H.; Han, C.C.; Hammouda, B. Concentration Fluctuations near Lower Critical Solution Temperature in Ternary Aqueous Solutions. *Macromolecules* **2017**, *50*, 7291–7298. [[CrossRef](#)]
91. Naim, A.B. *Molecular Theory of Solutions*; Oxford University Press: London, UK, 2006.
92. Marcus, Y. Preferential solvation in mixed solvents Part 8. Aqueous methanol from sub-ambient to elevated temperatures. *Phys. Chem. Chem. Phys.* **1999**, *1*, 2975–2983. [[CrossRef](#)]
93. Mukherji, D.; van der Vegt, N.F.A.; Kremer, K.; Delle Site, L. Kirkwood–Buff Analysis of Liquid Mixtures in an Open Boundary Simulation. *J. Chem. Theory Comput.* **2012**, *8*, 375–379. [[CrossRef](#)]
94. Sommer, J.U. Adsorption–Attraction Model for Co-Nonsolvency in Polymer Brushes. *Macromolecules* **2017**, *50*, 2219–2228. [[CrossRef](#)]
95. Sommer, J.U. Gluonic and Regulatory Solvents: A Paradigm for Tunable Phase Segregation in Polymers. *Macromolecules* **2018**, *51*, 3066–3074. [[CrossRef](#)]
96. Okada, Y.; Tanaka, F. Cooperative Hydration, Chain Collapse, and Flat LCST Behavior in Aqueous Poly(N-isopropylacrylamide) Solutions. *Macromolecules* **2005**, *38*, 4465–4471. [[CrossRef](#)]
97. Tanaka, F. Thermoreversible Gelation of Associating Polymers in Hydrogen-Bonding Mixed Solvents. *Langmuir* **2022**, *38*, 5098–5110. [[CrossRef](#)]
98. Mukherji, D.; Wagner, M.; Watson, M.D.; Winzen, S.; de Oliveira, T.E.; Marques, C.M.; Kremer, K. Reply to the ‘Comment on “Relating side chain organization of PNIPAm with its conformation in aqueous methanol”’ by A. Pica and G. Graziano, *Soft Matter*, 2017, 13,. *Soft Matter* **2017**, *13*, 7701–7703. [[CrossRef](#)]
99. Magda, J.J.; Fredrickson, G.H.; Larson, R.G.; Helfand, E. Dimensions of a polymer chain in a mixed solvent. *Macromolecules* **1988**, *21*, 726–732. [[CrossRef](#)]
100. Winnik, F.M.; Ottaviani, M.F.; Bossmann, S.H.; Garcia-Garibay, M.; Turro, N.J. Consolvency of poly(N-isopropylacrylamide) in mixed water-methanol solutions: A look at spin-labeled polymers. *Macromolecules* **1992**, *25*, 6007–6017. [[CrossRef](#)]
101. Wang, J.; Wang, N.; Liu, B.; Bai, J.; Gong, P.; Ru, G.; Feng, J. Preferential adsorption of the additive is not a prerequisite for consolvency in water-rich mixtures. *Phys. Chem. Chem. Phys.* **2017**, *19*, 30097–30106. [[CrossRef](#)]
102. Scholtz, J.; Barrick, D.; York, E.; Stewart, J.; Baldwin, R. Urea unfolding of peptide helices as a model for interpreting protein unfolding. *Proc. Natl. Acad. Sci. USA* **1995**, *92*, 185–189. [[CrossRef](#)]
103. Stumpe, M.C.; Grubmüller, H. Interaction of urea with amino acids: Implications for urea-induced protein denaturation. *J. Am. Chem. Soc.* **2007**, *129*, 16126–16131. [[CrossRef](#)]
104. Hua, L.; Zhou, R.; Thirumalai, D.; Berne, B.J. Urea denaturation by stronger dispersion interactions with proteins than water implies a 2-stage unfolding. *Proc. Natl. Acad. Sci. USA* **2008**, *105*, 16928–16933. [[CrossRef](#)] [[PubMed](#)]
105. Zangi, R.; Zhou, R.; Berne, B.J. Urea’s Action on Hydrophobic Interactions. *J. Am. Chem. Soc.* **2009**, *131*, 1535–1541. [[CrossRef](#)] [[PubMed](#)]
106. England, J.L.; Haran, G. Role of Solvation Effects in Protein Denaturation: From Thermodynamics to Single Molecules and Back. *Annu. Rev. Phys. Chem.* **2011**, *62*, 257–277. [[CrossRef](#)] [[PubMed](#)]
107. Elam, W.A.; Schrank, T.P.; Campagnolo, A.J.; Hilser, V.J. Temperature and urea have opposing impacts on polyproline II conformational bias. *Biochemistry* **2013**, *52*, 949–958. [[CrossRef](#)]
108. Raghunathan, S.; Jaganade, T.; Priyakumar, U.D. Urea-aromatic interactions in biology. *Biophys. Rev.* **2020**, *12*, 65–84. [[CrossRef](#)] [[PubMed](#)]
109. Bhatia, S.; Udgaonkar, J.B. Heterogeneity in Protein Folding and Unfolding Reactions. *Chem. Rev.* **2022**, *122*, 8911–8935. [[CrossRef](#)]
110. Baptista, L.A.; Zhao, Y.; Kremer, K.; Mukherji, D.; Cortes-Huerto, R. Stabilizing α -Helicity of a Polypeptide in Aqueous Urea: Dipole Orientation or Hydrogen Bonding? *ACS Macro Lett.* **2023**, *12*, 841–847. [[CrossRef](#)]
111. Konstantinovskiy, D.; Perets, E.A.; Santiago, T.; Velarde, L.; Hammes-Schiffer, S.; Yan, E.C.Y. Detecting the First Hydration Shell Structure around Biomolecules at Interfaces. *ACS Cent. Sci.* **2022**, *8*, 1404–1414. [[CrossRef](#)] [[PubMed](#)]
112. Kirkwood, J.G.; Buff, F.P. The Statistical Mechanical Theory of Solutions. I. *J. Chem. Phys.* **1951**, *19*, 774–777. [[CrossRef](#)]
113. Galata, A.A.; Anogiannakis, S.D.; Theodorou, D.N. Thermodynamic analysis of Lennard-Jones binary mixtures using Kirkwood–Buff theory. *Fluid Phase Equilibria* **2018**, *470*, 25–37. [[CrossRef](#)]
114. Sevilla, M.; Cortes-Huerto, R. Connecting density fluctuations and Kirkwood–Buff integrals for finite-size systems. *J. Chem. Phys.* **2022**, *156*, 044502. [[CrossRef](#)]
115. Kang, M.; Smith, P.E. Preferential interaction parameters in biological systems by Kirkwood–Buff theory and computer simulation. *Fluid Phase Equilibria* **2007**, *256*, 14–19. [[CrossRef](#)]

116. Kumari, P.; Pillai, V.V.S.; Gobbo, D.; Ballone, P.; Benedetto, A. The transition from salt-in-water to water-in-salt nanostructures in water solutions of organic ionic liquids relevant for biological applications. *Phys. Chem. Chem. Phys.* **2021**, *23*, 944–959. [[CrossRef](#)] [[PubMed](#)]
117. Forero-Martinez, N.C.; Cortes-Huerto, R.; Benedetto, A.; Ballone, P. Thermoresponsive Ionic Liquid/Water Mixtures: From Nanostructuring to Phase Separation. *Molecules* **2022**, *27*, 1647. [[CrossRef](#)] [[PubMed](#)]
118. Mukherji, D.; de Oliveira, T.E.; Ruscher, C.; Rottler, J. Thermodynamics, morphology, mechanics, and thermal transport of PMMA-PLA blends. *Phys. Rev. Mater.* **2022**, *6*, 025606. [[CrossRef](#)]
119. Venetsanos, F.; Anogiannakis, S.D.; Theodorou, D.N. Mixing Thermodynamics and Flory–Huggins Interaction Parameter of Polyethylene Oxide/Polyethylene Oligomeric Blends from Kirkwood–Buff Theory and Molecular Simulations. *Macromolecules* **2022**, *55*, 4852–4862. [[CrossRef](#)]
120. Müller, M.; Binder, K. An algorithm for the semi-grand-canonical simulation of asymmetric polymer mixtures. *Comput. Phys. Commun.* **1994**, *84*, 173–185. [[CrossRef](#)]
121. Krüger, P.; Schnell, S.K.; Bedeaux, D.; Kjelstrup, S.; Vlugt, T.J.H.; Simon, J.M. Kirkwood–Buff Integrals for Finite Volumes. *J. Phys. Chem. Lett.* **2013**, *4*, 235–238. [[CrossRef](#)] [[PubMed](#)]
122. Cortes-Huerto, R.; Kremer, K.; Potestio, R. Communication: Kirkwood–Buff integrals in the thermodynamic limit from small-sized molecular dynamics simulations. *J. Chem. Phys.* **2016**, *145*, 141103. [[CrossRef](#)]
123. Rösgen, J.; Pettitt, B.M.; Bolen, D.W. Protein Folding, Stability, and Solvation Structure in Osmolyte Solutions. *Biophys. J.* **2005**, *89*, 2988–2997. [[CrossRef](#)]
124. Hill, T.L. *An Introduction to Statistical Thermodynamics*; Courier Dover Publications: Mineola, NY, USA, 1960.
125. Wolf, B.A.; Blaum, G. Measured and calculated solubility of polymers in mixed solvents: Monotony and cosolvency. *J. Polym. Sci. Polym. Phys. Ed.* **1975**, *13*, 1115–1132. [[CrossRef](#)]
126. Yu, Y.; Kieviet, B.D.; Kutnyanszky, E.; Vancso, G.J.; de Beer, S. Cosolvency-Induced Switching of the Adhesion between Poly(methyl methacrylate) Brushes. *ACS Macro Lett.* **2015**, *4*, 75–79. [[CrossRef](#)]
127. Hoogenboom, R.; Becer, C.R.; Guerrero-Sanchez, C.; Hoepfner, S.; Schubert, U.S. Solubility and Thermoresponsiveness of PMMA in Alcohol–Water Solvent Mixtures. *Aust. J. Chem.* **2010**, *63*, 1173–1178. [[CrossRef](#)]
128. Lee, S.M.; Bae, Y.C. Enhanced solvation effect of re-collapsing behavior for cross-linked PMMA particle gel in aqueous alcohol solutions. *Polymer* **2014**, *55*, 4684–4692. [[CrossRef](#)]
129. Asadujjaman, A.; Ahmadi, V.; Yalcin, M.; ten Brummelhuis, N.; Bertin, A. Thermoresponsive functional polymers based on 2,6-diaminopyridine motif with tunable UCST behaviour in water/alcohol mixtures. *Polym. Chem.* **2017**, *8*, 3140–3153. [[CrossRef](#)]
130. Oyarte Gálvez, L.; de Beer, S.; van der Meer, D.; Pons, A. Dramatic effect of fluid chemistry on cornstarch suspensions: Linking particle interactions to macroscopic rheology. *Phys. Rev. E* **2017**, *95*, 030602. [[CrossRef](#)]
131. Mukherji, D.; Marques, C.M.; Stühn, T.; Kremer, K. Depleted depletion drives polymer swelling in poor solvent mixtures. *Nat. Commun.* **2017**, *8*, 1374. [[CrossRef](#)] [[PubMed](#)]
132. Lekkerkerker, H.N.W.; Tuinier, R. *Colloids and the Depletion Interaction*; Clarendon: Oxford, UK, 1990.
133. Mao, Y.; Cates, M.E.; Lekkerkerker, H.N.W. Depletion Stabilization by Semidilute Rods. *Phys. Rev. Lett.* **1995**, *75*, 4548–4551. [[CrossRef](#)]
134. Mao, Y.; Cates, M.; Lekkerkerker, H. Depletion force in colloidal systems. *Phys. A Stat. Mech. Its Appl.* **1995**, *222*, 10–24. [[CrossRef](#)]
135. Crocker, J.C.; Matteo, J.A.; Dinsmore, A.D.; Yodh, A.G. Entropic Attraction and Repulsion in Binary Colloids Probed with a Line Optical Tweezer. *Phys. Rev. Lett.* **1999**, *82*, 4352–4355. [[CrossRef](#)]
136. Phillips, R.; Kondev, J.; Theriot, J.; Garcia, H. *Physical Biology of the Cell*, 2nd ed.; Garland Science: New York, NY, USA, 2012.
137. Perera, A.; Sokolić, F.; Almásy, L.; Koga, Y. Kirkwood–Buff integrals of aqueous alcohol binary mixtures. *J. Chem. Phys.* **2006**, *124*, 124515. [[CrossRef](#)]
138. Chang, D.P.; Dolbow, J.E.; Zauscher, S. Switchable Friction of Stimulus-Responsive Hydrogels. *Langmuir* **2007**, *23*, 250–257. [[CrossRef](#)]
139. Lee, H.; Lee, B.P.; Messersmith, P.B. A reversible wet/dry adhesive inspired by mussels and geckos. *Nature* **2007**, *448*, 338–341. [[CrossRef](#)]
140. Schmidt, S.; Zeiser, M.; Hellweg, T.; Duschl, C.; Fery, A.; Moehwald, H. Adhesion and Mechanical Properties of PNIPAM Microgel Films and Their Potential Use as Switchable Cell Culture Substrates. *Adv. Funct. Mater.* **2010**, *20*, 3235–3243. [[CrossRef](#)]
141. Meddahi-Pellé, A.; Legrand, A.; Marcellan, A.; Louedec, L.; Letourneur, D.; Leibler, L. Organ Repair, Hemostasis, and In Vivo Bonding of Medical Devices by Aqueous Solutions of Nanoparticles. *Angew. Chem. Int. Ed.* **2014**, *53*, 6369–6373. [[CrossRef](#)] [[PubMed](#)]
142. de Beer, S.; Kutnyanszky, E.; Schön, P.M.; Vancso, G.J.; Muser, M.H. Solvent-induced immiscibility of polymer brushes eliminates dissipation channels. *Nat. Commun.* **2014**, *5*, 3781. [[CrossRef](#)]
143. Vogel, M.J.; Steen, P.H. Capillarity-based switchable adhesion. *Proc. Natl. Acad. Sci. USA* **2010**, *107*, 3377–3381. [[CrossRef](#)]
144. Mukherji, D.; Watson, M.D.; Morsbach, S.; Schmutz, M.; Wagner, M.; Marques, C.M.; Kremer, K. Soft and Smart: Co-nonsolvency-Based Design of Multiresponsive Copolymers. *Macromolecules* **2019**, *52*, 3471–3478. [[CrossRef](#)]
145. Arotçaréna, M.; Heise, B.; Ishaya, S.; Laschewsky, A. Switching the Inside and the Outside of Aggregates of Water-Soluble Block Copolymers with Double Thermoresponsivity. *J. Am. Chem. Soc.* **2002**, *124*, 3787–3793. [[CrossRef](#)]

146. Hietala, S.; Nuopponen, M.; Kalliomäki, K.; Tenhu, H. Thermoassociating Poly(N-isopropylacrylamide) A-B-A Stereoblock Copolymers. *Macromolecules* **2008**, *41*, 2627–2631. [[CrossRef](#)]
147. Plamper, F.A.; Steinschulte, A.A.; Hofmann, C.H.; Drude, N.; Mergel, O.; Herbert, C.; Erberich, M.; Schulte, B.; Winter, R.; Richtering, W. Toward Copolymers with Ideal Thermosensitivity: Solution Properties of Linear, Well-Defined Polymers of N-Isopropyl Acrylamide and N,N-Diethyl Acrylamide. *Macromolecules* **2012**, *45*, 8021–8026. [[CrossRef](#)]
148. Yin, F.; Laborie, P.; Lonetti, B.; Gineste, S.; Coppel, Y.; Lauth-de Viguier, N.; Marty, J.D. Dual Thermo- and pH-Responsive Block Copolymer of Poly(N-isopropylacrylamide)-block-Poly(N,N-diethylamino Ethyl Acrylamide): Synthesis, Characterization, Phase Transition, and Self-Assembly Behavior in Aqueous Solution. *Macromolecules* **2023**, *56*, 3703–3720. [[CrossRef](#)]
149. Ko, C.H.; Henschel, C.; Meledam, G.P.; Schroer, M.A.; Guo, R.; Gaetani, L.; Müller-Buschbaum, P.; Laschewsky, A.; Papadakis, C.M. Co-Nonsolvency Effect in Solutions of Poly(methyl methacrylate)-b-poly(N-isopropylacrylamide) Diblock Copolymers in Water/Methanol Mixtures. *Macromolecules* **2021**, *54*, 5825–5837. [[CrossRef](#)]
150. Henry, A. Thermal transport in polymers. *Annu. Rev. Heat Transf.* **2014**, *17*, 485–520. [[CrossRef](#)]
151. Kim, G.; Lee, D.; Shanker, A.; Shao, L.; Kwon, M.S.; Gidley, D.; Kim, J.; Pipe, K.P. High thermal conductivity in amorphous polymer blends by engineered interchain interactions. *Nat. Mater.* **2015**, *14*, 295–300. [[CrossRef](#)]
152. Xie, X.; Li, D.; Tsai, T.; Liu, J.; Braun, P.V.; Cahill, D.G. Thermal Conductivity, Heat Capacity, and Elastic Constants of Water-Soluble Polymers and Polymer Blends. *Macromolecules* **2016**, *49*, 972–978. [[CrossRef](#)]
153. Bruns, D.; de Oliveira, T.E.; Rottler, J.; Mukherji, D. Tuning Morphology and Thermal Transport of Asymmetric Smart Polymer Blends by Macromolecular Engineering. *Macromolecules* **2019**, *52*, 5510–5517. [[CrossRef](#)]
154. Koblinski, P. Modeling of Heat Transport in Polymers and Their Nanocomposites. In *Handbook of Materials Modeling*; Springer International Publishing: Cham, Switzerland, 2020; pp. 975–997.
155. Smith, M.K.; Singh, V.; Kalaitzidou, K.; Cola, B.A. High Thermal and Electrical Conductivity of Template Fabricated P3HT/MWCNT Composite Nanofibers. *ACS Appl. Mater. Interfaces* **2016**, *8*, 14788–14794. [[CrossRef](#)] [[PubMed](#)]
156. Shi, W.; Shuai, Z.; Wang, D. Tuning Thermal Transport in Chain-Oriented Conducting Polymers for Enhanced Thermoelectric Efficiency: A Computational Study. *Adv. Funct. Mater.* **2017**, *27*, 1702847. [[CrossRef](#)]
157. Cahill, D.G.; Watson, S.K.; Pohl, R.O. Lower Limit to the Thermal Conductivity of Disordered Crystals. *Phys. Rev. B* **1990**, *46*, 6131–6140. [[CrossRef](#)] [[PubMed](#)]
158. Cahill, D.G.; Ford, W.K.; Goodson, K.E.; Mahan, G.D.; Majumdar, A.; Maris, H.J.; Merlin, R.; Phillpot, S.R. Nanoscale Thermal Transport. *J. Appl. Phys.* **2003**, *93*, 793–818. [[CrossRef](#)]
159. Olson, J.R.; Topp, K.A.; Pohl, R.O. Specific Heat and Thermal Conductivity of Solid Fullerenes. *Science* **1993**, *259*, 1145–1148. [[CrossRef](#)] [[PubMed](#)]
160. Ren, S.; Bernardi, M.; Lunt, R.R.; Bulovic, V.; Grossman, J.C.; Gradecak, S. Toward Efficient Carbon Nanotube/P3HT Solar Cells: Active Layer Morphology, Electrical, and Optical Properties. *Nano Lett.* **2011**, *11*, 5316–5321. [[CrossRef](#)]
161. Fugallo, G.; Colombo, L. Calculating Lattice Thermal Conductivity: A Synopsis. *Phys. Scr.* **2018**, *93*, 043002. [[CrossRef](#)]
162. Braun, J.L.; Rost, C.M.; Lim, M.; Giri, A.; Olson, D.H.; Kotsonis, G.N.; Stan, G.; Brenner, D.W.; Maria, J.P.; Hopkins, P.E. Charge-Induced Disorder Controls the Thermal Conductivity of Entropy-Stabilized Oxides. *Adv. Mater.* **2018**, *30*, 1805004. [[CrossRef](#)] [[PubMed](#)]
163. Shen, S.; Henry, A.; Tong, J.; Zheng, R.; Chen, G. Polyethylene nanofibres with very high thermal conductivities. *Nat. Nanotechnol.* **2010**, *5*, 251–255. [[CrossRef](#)]
164. Tomko, J.A.; Pena-Francesch, A.; Jung, H.; Tyagi, M.; Allen, B.D.; Demirel, M.C.; Hopkins, P.E. Tunable thermal transport and reversible thermal conductivity switching in topologically networked bio-inspired materials. *Nat. Nanotechnol.* **2018**, *13*, 959–964. [[CrossRef](#)] [[PubMed](#)]
165. Li, C.; Ma, Y.; Tian, Z. Thermal Switching of Thermo-responsive Polymer Aqueous Solutions. *ACS Macro Lett.* **2018**, *7*, 53–58. [[CrossRef](#)]
166. Feng, H.; Tang, N.; An, M.; Guo, R.; Ma, D.; Yu, X.; Zang, J.; Yang, N. Thermally-Responsive Hydrogels Poly(N-Isopropylacrylamide) as the Thermal Switch. *J. Phys. Chem. C* **2019**, *123*, 31003–31010. [[CrossRef](#)]
167. Mukherji, D.; Singh, M.K. Tuning thermal transport in highly cross-linked polymers by bond-induced void engineering. *Phys. Rev. Mater.* **2021**, *5*, 025602. [[CrossRef](#)]
168. Lv, G.; Jensen, E.; Evans, C.M.; Cahill, D.G. High Thermal Conductivity Semicrystalline Epoxy Resins with Anthraquinone-Based Hardeners. *ACS Appl. Polym. Mater.* **2021**, *3*, 4430–4435. [[CrossRef](#)]
169. Maurya, M.K.; Wu, J.; Singh, M.K.; Mukherji, D. Thermal Conductivity of Semicrystalline Polymer Networks: Crystallinity or Cross-Linking? *ACS Macro Lett.* **2022**, *11*, 925–929. [[CrossRef](#)]
170. Zheng, R.; Gao, J.; Wang, J.; Chen, G. Reversible temperature regulation of electrical and thermal conductivity using liquid–solid phase transitions. *Nat. Commun.* **2011**, *2*, 289. [[CrossRef](#)]
171. Tang, N.; Peng, Z.; Guo, R.; An, M.; Chen, X.; Li, X.; Yang, N.; Zang, J. Thermal Transport in Soft PAAm Hydrogels. *Polymers* **2017**, *9*, 688. [[CrossRef](#)]
172. Pallecchi, E.; Chen, Z.; Fernandes, G.E.; Wan, Y.; Kim, J.H.; Xu, J. A thermal diode and novel implementation in a phase-change material. *Mater. Horiz.* **2015**, *2*, 125–129. [[CrossRef](#)]
173. Wu, J.; Mukherji, D. Comparison of all atom and united atom models for thermal transport calculations of amorphous polyethylene. *Comput. Mater. Sci.* **2022**, *211*, 111539. [[CrossRef](#)]

174. Shenogin, S.; Bodapati, A.; Keblinski, P.; McGaughey, A.J.H. Predicting the thermal conductivity of inorganic and polymeric glasses: The role of anharmonicity. *J. Appl. Phys.* **2009**, *105*, 034906. [[CrossRef](#)]
175. Simavilla, D.N.; Sgouros, A.P.; Vogiatzis, G.; Tzoumanekas, C.; Georgilas, V.; Verbeeten, W.M.H.; Theodorou, D.N. Molecular Dynamics Test of the Stress-Thermal Rule in Polyethylene and Polystyrene Entangled Melts. *Macromolecules* **2020**, *53*, 789–802. [[CrossRef](#)]
176. Ruscher, C.; Rottler, J.; Boott, C.E.; MacLachlan, M.J.; Mukherji, D. Elasticity and thermal transport of commodity plastics. *Phys. Rev. Mater.* **2019**, *3*, 125604. [[CrossRef](#)]
177. Charlier, J.C.; Blase, X.; Roche, S. Electronic and transport properties of nanotubes. *Rev. Mod. Phys.* **2007**, *79*, 677–732. [[CrossRef](#)]
178. Gottlieb, S.; Pigard, L.; Ryu, Y.K.; Lorenzoni, M.; Evangelio, L.; Fernández-Regúlez, M.; Rawlings, C.D.; Spieser, M.; Perez-Murano, F.; Müller, M.; et al. Thermal Imaging of Block Copolymers with Sub-10 nm Resolution. *ACS Nano* **2021**, *15*, 9005–9016. [[CrossRef](#)]
179. Pigard, L.; Mukherji, D.; Rottler, J.; Müller, M. Microscopic Model to Quantify the Difference of Energy-Transfer Rates between Bonded and Nonbonded Monomers in Polymers. *Macromolecules* **2021**, *54*, 10969–10983. [[CrossRef](#)]
180. Bhardwaj, A.; Phani, A.S.; Nojeh, A.; Mukherji, D. Thermal Transport in Molecular Forests. *ACS Nano* **2021**, *15*, 1826–1832. [[CrossRef](#)]
181. Crist, B.; Hereña, P.G. Molecular orbital studies of polyethylene deformation. *J. Polym. Sci. Part B Polym. Phys.* **1996**, *34*, 449–457. [[CrossRef](#)]
182. Hsu, H.P.; Singh, M.K.; Cang, Y.; Thérien-Aubin, H.; Mezger, M.; Berger, R.; Lieberwirth, I.; Fytas, G.; Kremer, K. Free Standing Dry and Stable Nanoporous Polymer Films Made through Mechanical Deformation. *Adv. Sci.* **2023**, *10*, 2207472. [[CrossRef](#)]
183. Lv, G.; Jensen, E.; Shen, C.; Yang, K.; Evans, C.M.; Cahill, D.G. Effect of Amine Hardener Molecular Structure on the Thermal Conductivity of Epoxy Resins. *ACS Appl. Polym. Mater.* **2021**, *3*, 259–267. [[CrossRef](#)]
184. Lv, G.; Soman, B.; Shan, N.; Evans, C.M.; Cahill, D.G. Effect of Linker Length and Temperature on the Thermal Conductivity of Ethylene Dynamic Networks. *ACS Macro Lett.* **2021**, *10*, 1088–1093. [[CrossRef](#)]
185. Wei, X.; Luo, T. Role of Ionization in Thermal Transport of Solid Polyelectrolytes. *J. Phys. Chem. C* **2019**, *123*, 12659–12665. [[CrossRef](#)]
186. Hsieh, W.P.; Losego, M.D.; Braun, P.V.; Shenogin, S.; Keblinski, P.; Cahill, D.G. Testing the minimum thermal conductivity model for amorphous polymers using high pressure. *Phys. Rev. B* **2011**, *83*, 174205. [[CrossRef](#)]
187. Lv, G.; Shen, C.; Shan, N.; Jensen, E.; Li, X.; Evans, C.M.; Cahill, D.G. Odd–even effect on the thermal conductivity of liquidcrystalline epoxy resins. *Proc. Natl. Acad. Sci. USA* **2022**, *119*, e2211151119. [[CrossRef](#)] [[PubMed](#)]
188. Lim, M.; Rak, Z.; Braun, J.L.; Rost, C.M.; Kotsonis, G.N.; Hopkins, P.E.; Maria, J.P.; Brenner, D.W. Influence of mass and charge disorder on the phonon thermal conductivity of entropy stabilized oxides determined by molecular dynamics simulations. *J. Appl. Phys.* **2019**, *125*, 055105. [[CrossRef](#)]
189. Ahmed, J.; Wang, Q.J.; Balogun, O.; Ren, N.; England, R.; Lockwood, F. Molecular Dynamics Modeling of Thermal Conductivity of Several Hydrocarbon Base Oils. *Tribol. Lett.* **2023**, *71*, 70. [[CrossRef](#)]
190. Gao, H.; Menzel, T.P.W.; Müser, M.H.; Mukherji, D. Comparing simulated specific heat of liquid polymers and oligomers to experiments. *Phys. Rev. Mater.* **2021**, *5*, 065605. [[CrossRef](#)]
191. Bhowmik, R.; Sihn, S.; Varshney, V.; Roy, A.K.; Vernon, J.P. Calculation of specific heat of polymers using molecular dynamics simulations. *Polymer* **2019**, *167*, 176–181. [[CrossRef](#)]
192. Demydiuk, F.; Solar, M.; Meyer, H.; Benzerara, O.; Paul, W.; Baschnagel, J. Role of torsional potential in chain conformation, thermodynamics, and glass formation of simulated polybutadiene melts. *J. Chem. Phys.* **2022**, *156*, 234902. [[CrossRef](#)] [[PubMed](#)]
193. Horbach, J.; Kob, W.; Binder, K. Specific Heat of Amorphous Silica within the Harmonic Approximation. *J. Phys. Chem. B* **1999**, *103*, 4104–4108. [[CrossRef](#)]
194. Yu, Y.; Brió Pérez, M.; Cao, C.; de Beer, S. Switching (bio-) adhesion and friction in liquid by stimulus responsive polymer coatings. *Eur. Polym. J.* **2021**, *147*, 110298. [[CrossRef](#)]

Disclaimer/Publisher’s Note: The statements, opinions and data contained in all publications are solely those of the individual author(s) and contributor(s) and not of MDPI and/or the editor(s). MDPI and/or the editor(s) disclaim responsibility for any injury to people or property resulting from any ideas, methods, instructions or products referred to in the content.